MARS-CT: Biomedical Spectral X-ray Imaging with Medipix

A thesis
submitted in fulfilment
of the requirements for a Certificate of Proficiency
for
the MDPH690 MSc thesis
at the
University of Canterbury
by

Jochen S. Butzer

Supervisors
Prof. Phil Butler (University of Canterbury, Christchurch, New Zealand)
Prof. Tilo Baumbach (Karlsruhe Institute of Technology, Karlsruhe, Germany)
Dr. Anthony Butler (Christchurch School of Medicine, Christchurch, New Zealand)
Prof. Phil Bones (University of Canterbury, Christchurch, New Zealand)

University of Canterbury
2009

Abstract

Computed Tomography is one of the most important image modalities in medical imaging nowadays. Recent developements have led to a new acquisition technique called 'dual-energy', where images are taken with different x-ray spectra. This enables for the first time spectral information in the CT dataset. Our approach was to use an energy resolving detector (Medipix) and investigate its potential in the medical imaging domain. Images are taken in different energy bins. For acquisition of the data, a CT scanner called 'Medipix All Resolution System' (MARS) scanner was constructed. It was upgraded to achieve better image quality as well as faster scan time and a stable operation.

In medical imaging, it is important to achieve a high contrast and a good detail recognition at a low dose. Therefore, it is common practice to use contrast agents to highlight certain regions of the body like e.g. the vascular system. But with a broad spectrum acquisition, it is often impossible to distinguish highly absorbing body elements like bones from the contrast agent. We target this problem by a contrast agent study using different energy bins. This so called spectral contrast agent study has been conducted with small animals using the MARS scanner. The data has been processed to create an optimal CT reconstruction. The image enhancement techniques consist of corrections for noisy pixels, intensity fluctuations and eliminating streaks in the sinograms to reduce ring artifacts.

In order to evaluate the data, we used two methods of material identification. The material reconstruction method works on projection data and uses a maximum-likelihood estimation to reconstruct images of base materials. The second method, the principal component analysis (PCA), identifies the relevant information from the spectral dataset in a few derived variables that account for most of the variance in the dataset. This resulted in images with enhanced contrast and removed redundancies. It is possible to combine these images in one colour image where anatomical structures are shown in good detail and certain materials show up in different colours. Based on this new information from spectral data, we could show that it is possible to distinguish the spinal bone from contrast agent.

Table of Contents

Chapter I

Introduction

1.1 Motivation for spectral imaging

It was on the 8th of November 1895 that Conrad Wilhelm Roentgen first discovered x-rays. A few weeks later, he imaged his wife's hand which became known as the first medical x-ray image. The technique of x-ray imaging soon was introduced into medical applications and is still important today.

Over the last decades, especially with advances in computers, new methods for x-ray imaging have been developed. One of the most important ones is computed tomography (CT) invented by Hounsfield in 1972. In CT, 2D projections are acquired from different angles and via the inverse Radon-transform, this dataset of pixels is used to compute 3D voxels of the object. It is common practice to arrange the voxels to images of slices through the object.

Despite the advances in CT, the x-ray detector remains the weakest part of the imaging chain making developement in this area essential. Our research focuses on a new type of detector, the photon processing chip Medipix. In contrast to the commonly used integrating detector where the registered signal is proportional to the deposited energy, Medipix is capable of processing each incoming x-ray photon individually. It allows the user to specify an energy window within which x-ray photons are counted. This enables a new imaging mode: Spectral x-ray imaging.

Shortly before my starting on the project, the MARS group at University of Canterbury together with physicists from Christchurch Hospital constructed a Medipix based CT scanner. With this scanner, images are taken not only from different angles as in CT, but also in different energy bins. Because of the new energy resolution that Medipix provides, our system was

dubbed 'Medipix All Resolution System' (MARS).

Currently, there exists another method in clinical use that offers some energy information. It is called 'dual-energy', as typically two acquisitions from different x-ray spectra are used. Each acquisition provides different information as the attenuation of the material is dependent on the energy of the x-rays.

There are several applications for dual-energy which range from mammography [Asaga et al., 1987] to angiography [Scheffel et al., 2006] and abdominal imaging [Graser et al., 2008]. The contrast from both contrast agents and intrinsic contrast can be optimised for example between breast tumour tissue and soft tissue [Asaga et al., 1987]. Furthermore, it is proposed that artefacts can be reduced [Bisogni et al., 2007] and material properties like the chemical composition of lesions can be better characterised [Johnson et al., 2007]. Additionally, it is possible to perform multiphase studies, which typically involve multiple exposures, in only one acquisition thus reducing dose, resources, alignment artefacts and scan time [Zhang et al., 2008].

All the above applications demonstrate the potential of spectral imaging and most of the benefits are also relevant for MARS-CT. Medical applications of the Medipix technology in clinical studies include angiographic imaging [Fanti et al., 2003], mammography [Blanchot et al., 2006] and [Bisogni et al., 2002] as well as radionuclide imaging in small animals [Autiero et al., 2005]. Other spectral CT scanners [Gleason et al., 1999] and medical applications of other multi-energy detectors [Bollini et al., 2003] have shown promising results. With a photon processing detector, an optimised energy weighting can be introduced [Giersch et al., 2004] which improves the signal-to-noise ratio (SNR) and thus allows imaging at a lower dose with the same SNR.

This thesis describes aspects of the development of MARS-CT and first biomedical contrast agent studies.

The use of contrast agents in medical x-ray imaging allows one to highlight certain anatomic details such as for example the vascular system. However in acquisitions where a broad energy spectrum is recorded, the intensity of contrast agent and bone material or between two contrast agents is sometimes similar. In this thesis, I investigate the advantages from the additional energy

information that a photon-processing detector offers. It is used to isolate and highlight different materials.

With such a new detector technology, it is important to develop adequate image correction techniques. Furthermore, this spectroscopic dataset provides new information that has to be evaluated by new methods. Both has been performed in the work of this thesis.

Chapter II starts with a description of the Medipix technology, equalisation and calibration of the chip. Then the 'Medipix All Resolution System' (MARS) scanner in its first version is described. Key components are presented and their suitability is discussed. The last part of the chapter describes the upgrade of the scanner to the configuration which became known as 'MARS-2'. Key goals of the upgrade were stability, faster scan time, better accuracy and improved image quality.

Having described the hardware, Chapter III focuses on improving the first datasets from contrast agent studies. The image correction techniques aim at reducing fluctuations, removing noise and correcting uneven pixel responses. The latter has been further optimised with a routine that reduces ring-artefacts. As a last step, a cone-beam filtered backprojection is applied. The resulting slices in all energy bins are then able to be evaluated.

Chapter IV describes two methods for evaluating the spectral information contained in the data. The first method works on the raw data. It uses a maximum-likelihood estimation to reconstruct projections of base materials [Firsching, 2005]. These are then corrected by the methods described in Chapter III and result in CT slices representing the partial density of the base materials. In addition, we have introduced a new technique, the method of principal component analysis (PCA). It aims at maximising the variance in the dataset by transforming it onto a base spanned by linearly independent components. The method is first tested on radiographic datasets before it is applied to CT slices from different energy bins.

Chapter V reports on results from the contrast agent studies of biomedical subjects. Visible biological structures are described and images from the PCA method and the material reconstruction are discussed.

The configuration and upgrade of the scanner has been presented at the IEEE Medical Imaging Conference in October 2008 in Dresden, Germany; a

talk at the 'Engineering and Physical Sciences in Medicine and the Australian Biomedical Engineering Conference' in November 2008, Christchurch, New Zealand focussed on the results from the first contrast agent studies.

Applying the method of PCA to Medipix imaging has been presented at the 23rd International Conference on Image and Vision Computing New Zealand held in November 2008 in Christchurch, New Zealand. Furthermore, work on the PCA method has contributed to a publication which will be presented at the 'Society for Imaging Informatics in Medicine' annual meeting which takes place in Charlotte, NC, USA in June 2009.

Aspects of the work have contributed to publications and presentation on the 'International Symposium on Peaceful Applications of Nuclear Technologies in the GCC Countries' which was held in Jeddah, Saudi-Arabia in November 2008 and the 'European Society of Radiology' congress which took place in Vienna, Austria in March 2009.

1.2 Physical background

1.2.1 Creation of x-rays

In an x-ray tube, electrons which are created at the cathode are accelerated towards the anode. When they hit the anode material (in our case Tungsten), mainly two physical effects which create x-rays take place: Bremsstrahlung and characteristic radiation. Bremsstrahlung is produced, when the electrons have passed the outer shells without interaction and are decelerated in the field of the nucleus of the target material. Characteristic radiation results from interactions between the accelerated electron and an inner shell electron which is knocked out. Its place is filled by an electron from another shell considering the selection rules. The discrete transition energies are characteristic for the target material used and show as peaks in the x-ray spectra.

The spectrum from an x-ray tube contains contributions from both the characteristic radiation and Bremsstrahlung. In section 2.2.2 the x-ray spectrum from the used x-ray tube is simulated. Typical x-ray peak energies used in medical imaging range from 30 to 150 keV.

The efficiency of x-ray tubes is given by $\eta = k \cdot U_A \cdot Z$ with $k \approx 1 \cdot 10^{-9}\, V^{-1}$ [Doessel, 2000]. For tungsten (Z = 74) and $U_A = 100\,\mathrm{kV}$ this results in

$\eta = 0.7\,\%$, which means that 99.3% of the input power results in heat. This causes problems with heat dissipation especially at small focal spot sizes and thus limits the output photon flux. One possible solution which is often used in medical applications is a rotating anode where the heat is dissipated over a larger area.

1.2.2 Interaction of x-rays with matter

As x-rays pass through matter with thickness x the intensity decreases exponentially. This is given by the law of Lambert-Beer: $I = I_0 \cdot e^{-\mu x}$ where μ is the attenuation coefficient and I_0 the incident intensity. The attenuation is caused by different types of interaction of the x-ray quantums and the atoms such as scattering and absorption.

X-ray quantums can be absorbed by electrons in inner atomic shells. Thus the atom is ionized, an effect called the photoelectric effect. For energies above the ionisation energy of the K-shell, a new channel of interaction is possible, resulting in a higher absorbtion. The energy at which this effect occurs is called k-edge or accordingly l-edge for electrons from the L-shell.

The Compton effect describes the inelastic and incoherent scattering of the photon at an electron of the outer shell. The energy of the photon decreases and its wavelength increases by $\Delta\lambda$. It is scattered under the angle Φ according to the equation:

$$\Delta\lambda = \frac{h}{m_e c}(1 - cos\Phi)$$

where m_e is the electron mass, h is Plancks constant.

Additionally, coherent scattering of the photon can occur where incident and scattered photon show a fixed phase correlation. As this is an elastic scattering process, only the direction of the photon is changed but no energy is transmitted. The two types that can occur, dependant on the size of the scattering center in relation to the wavelength of the incident photon, are the Thomson scattering and Rayleight scattering.

For energies above 1.02 MeV, which is two rest masses of an electron, pair production is possible. The resulting electron and positron have the same kinetic energy E_{kin}. The atoms can provide for momentum and energy

conservation.

Considering all these interactions, the attenuation coefficient can be written as:

$$\mu = \mu_{scatter} + \mu_{photo} + \mu_{Compton} + \mu_{pair}$$

1.2.3 Dependence of the absorption coefficient on energy and material

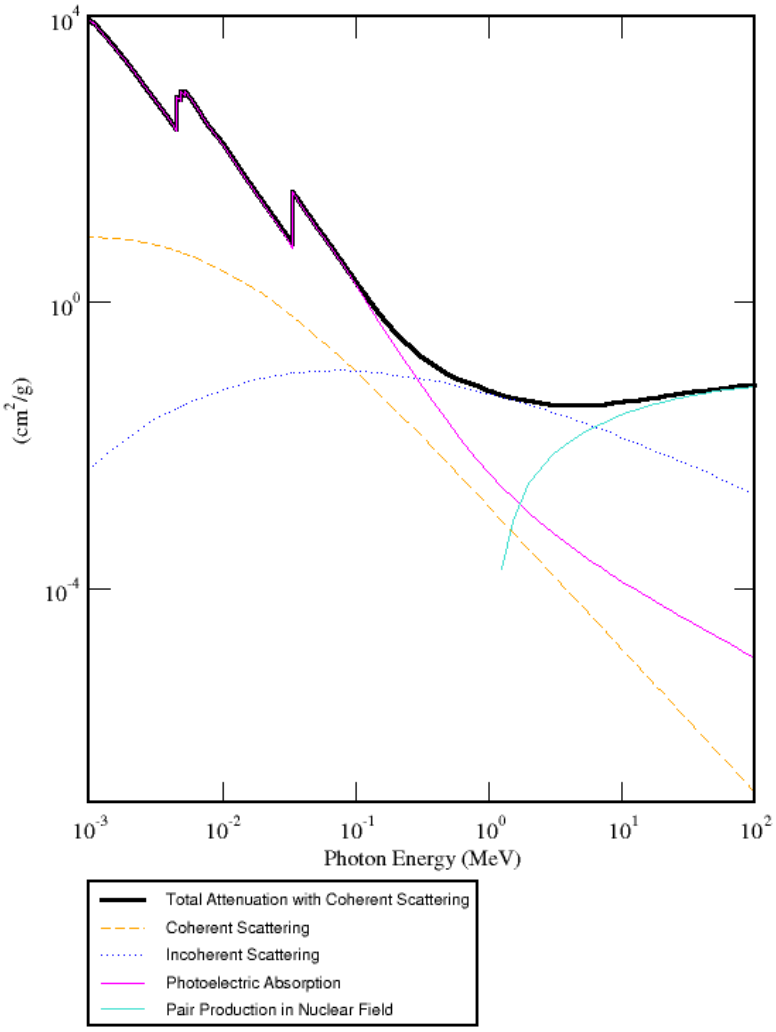

Figure 1.1: Different effects that contribute to the attenuation in the object (in this case iodine).

Figure 1.1 shows the dependence of the absorption coefficient on the en-

ergy in Iodine. Dominant effects are the photo-electric effect for energies in the range of keV, the Compton effect in the range of MeV and the pair production for high energy experiments. Thus, the main absorption effects of x-ray quantums in matter in our case are the photo effect and Compton effect (incoherent scattering), as the energy is too low for pair production and the contribution from coherent scattering is neglectable. The photo effect follows a E^{-k} dependency with values for k between 3 and 4 [Firsching, 2005]. K- and L-edges are also visible. The Compton effect is generally described by the Klein-Nishina equation. However, for the energy range used in medical imaging, $\mu_{Compton}$ can be seen as independant of E.

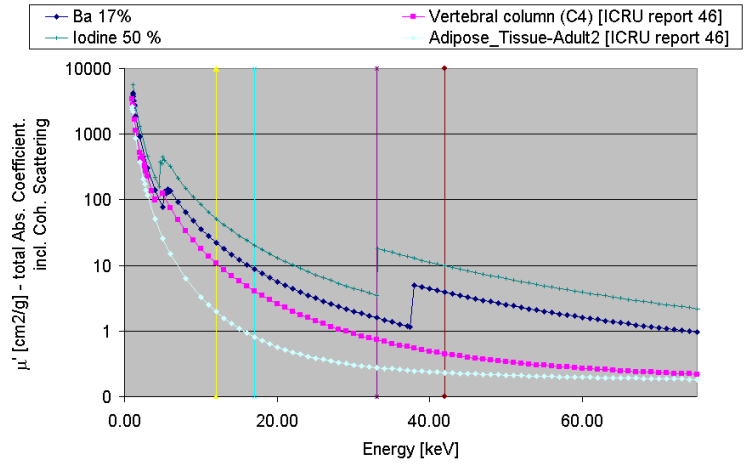

Figure 1.2: Mass attenuation coefficient for different materials plotted against photon energy.

In figure 1.2, the energy-dependency of the mass attenuation coefficient is shown for different materials. We chose a 17 % barium and a 50 % iodine solution in water as well as average adipose tissue and the spinal bone C4. The data for the composition of the body tissues has been taken from the report 46 of the International Comission on Radiation Units & Measurements (ICRU). From this information, the mass attenuation has been simulated using the XCOM program from the National Institute of Standards and Technology (NIST). It can be seen that each material has its individual characteristic curve. Especially the k-edge of the two contrast agents is clearly visible. All

materials show a steeper slope for lower energies where the photoelectric effect is dominating. The mass attenuation coefficient depends on the atomic number and is proportional to Z^3 for the photoelectric effect. The Compton effect is independant of the atomic number, but gives a measure for the electron density.

1.2.4 Spectral imaging chain

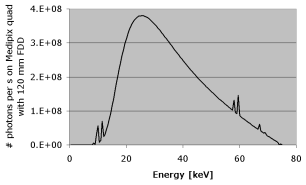

(a) X-ray tube spectrum $I(E)$ - see figure 2.9

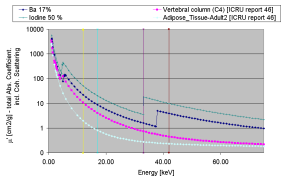

(b) Attenuation coefficient $\mu(E)$ for different materials - see figure 1.2

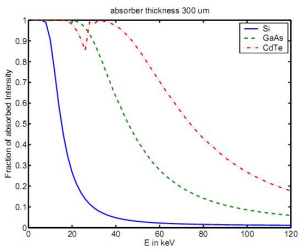

(c) Detection efficiency D(E) for different sensor materials - see figure 2.1

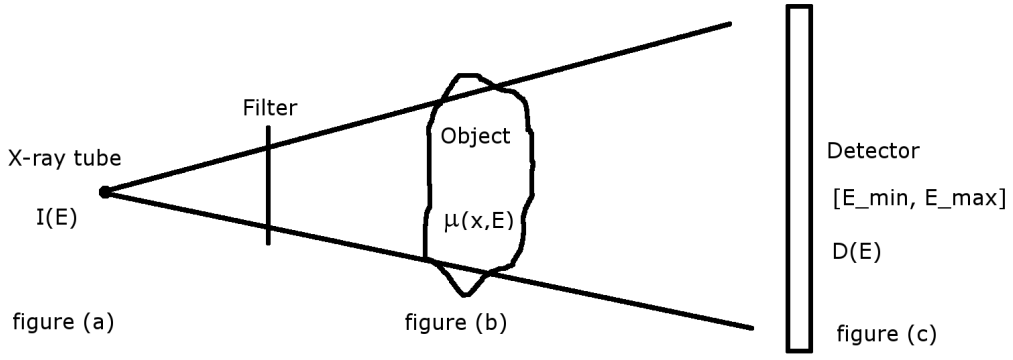

(d) Spectral imaging chain

Figure 1.3: Different energy dependencies in the x-ray imaging chain.

In conclusion, we summarise the different energy-dependant parts in the imaging chain as shown from the sketch in figure 1.3.

Photons are created in the x-ray tube with a characteristic intensity distribution or spectrum $I(E)$. They are transmitted through the object where different materials have an energy dependent attenuation coefficient $\mu(E)$. Finally they are detected in the sensor where they are counted if they are within a specified energy bin $[E_{min}, E_{max}]$. The detection efficiency $D(E)$ is dependent on the energy of the photon.

It is possible, to utilise these energy-dependencies in various ways.

The x-ray spectrum $I(E)$ can be altered by the use of filter materials in which especially lower energy photons are absorbed. It is used to reduce the amount of scattered radiation and in addition to decrease the dose delivered to the patient. To further change the spectrum, a different x-ray voltage can be specified. This is used in dual-energy imaging where two acquisitions from different x-ray spectra are taken.

As shown before, different materials have different characteristic attenuation coefficients $\mu(E)$. These have contributions from different physical effects such as the photoelectric effect or the Compton effect. The transmittance $T(E)$ is given by $T(E) = e^{-\int \mu(E,x)dx}$. Using contrast agents, it is possible to increase the contrast and to highlight certain anatomical structures. In general, it is also possible to consider the phase contrast from the transmitted wave. In our case, this is not practicable, as the x-ray tube creates an incoherent radiation.

For the Medipix detector, specifying an energy window $[E_{min}, E_{max}]$ in which the incident photons are counted allows energy-discriminative measurements. The contrast between different materials can be optimised by the selection of the optimal energy bin. Often, this is posssible by imaging near or at the k-edge of a contrast agent - this is called k-edge imaging. The detection efficiency $D(E)$ of the sensor material is energy dependent - for silicon, it is reduced to a few percent for energies above 30 keV. It can be optimised for higher energies by the use of high-Z materials such as GaAs or CdTe. In dual energy imaging, specific detectors have been developed that compromise two sensors behind each other where one registers the low and the other one the high energy part of the incoming intensity.

In our case, we made use of the different characteristic attenuation coefficients, especially by the use of contrast agent and by the use of different

energy windows. Methods for the evalutation of this energy information are part of this thesis.

Chapter II

The 'Medipix All Resolution System' (MARS)

The aim of this chapter is to describe the Medipix technology and its implementation into a series of CT scanners built in Christchurch. The first version of the scanner, MARS-1, was operational from late 2007 till April 2008. Experience and feedback from evaluation of the first data led to a review of the design and motivated an upgrade of the configuration and software which became known as MARS-2. It has been operational since August 2008. The design of the next version of the scanner (MARS-3) is discussed briefly.

2.1 Medipix technology

Medipix is a photon-processing pixel detector allowing energy selective imaging. An energy window can be specified and photon arrival events are counted for each pixel if they are within this energy range. The window is specified by a low energy threshold (THL) and a high energy threshold (THH). Both are set as values of the digital-to-analog converter (DAC) on the chip. The THH value can be deactivated by choosing THH < THL. The Medipix chip is a hybrid detector, consisting of complementary metal oxide semiconductor (CMOS) electronics bump-bonded to a layer of semiconductor sensor material. The sensor material can vary for different applications. For x-ray detection, typically silicon is used due to its wide availability in good quality. However, other materials like GaAs and CdTe have also been realized and tested [Mitschke, 2006]. These show a higher detection efficiency especially for energies above 30 keV (figure 2.1). Neutron detection is also possible with an additional layer of a converter material such as ^{6}LiF, where the interaction between neutrons and the converter material creates heavy particles that can

then be detected [Uher et al., 2008].

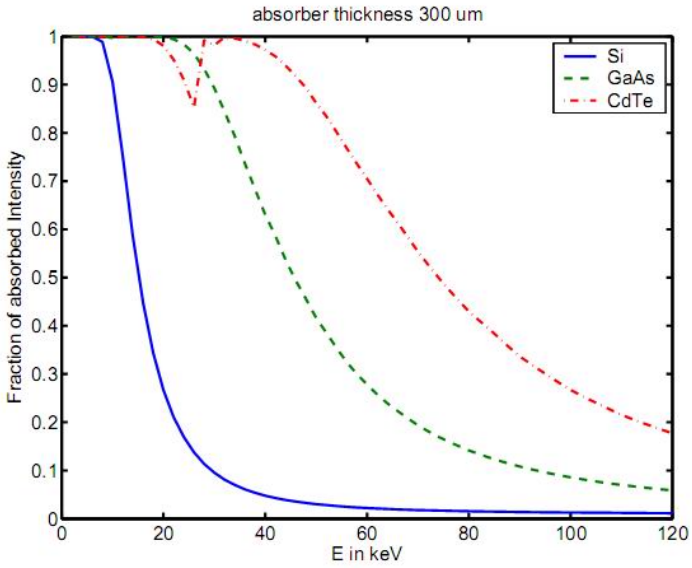

Figure 2.1: Absorption of a photon beam in a 300 μm slab of Si, GaAs and CdTe as a function of the photon energy. [Mitschke, 2006]

History

The Medipix detectors are being developed and tested by a collaboration of universities and research institutes worldwide which gives a great opportunity to share ideas and experience. There are several collaborations for different versions of the detector. The group at University of Canterbury is part of the Medipix-3 collaboration. The microelectronics group at CERN has been designing hybrid pixel detectors since 1990 [Campbell et al., 1990]. The first version of the Medipix chip 'Medipix-1' was constructed in 1998 with a focus on evaluating the potential of hybrid pixel detectors for imaging applications [Campbell et al., 1998]. It consisted of 64 by 64 pixels each of the size of 170 μm by 170 μm. While Medipix-1 served as a proof of concept, the second version, Medipix-2 was built in 2001. With advances in CMOS processing, it was possible to decrease the pixel size to $55 \times 55\,\mu\text{m}^2$ and to add new functionality to the chip. A photo of a Medipix-2 detector can be seen in

figure 2.2. An upgrade of the Medipix-2 chip became known as the MXR version. The counter depth has been upgraded from 8192 (13 bit) to 11810 and the DAC values are now set on a 10 bit range rather than 8 bit. Some members of the collaboration have temperature stabilised the MXR chip via a heat sink mounted on the back of the readout electronics. This eliminates problems caused by the temperature dependency of the energy calibration values during operation [Ewald, 2007].

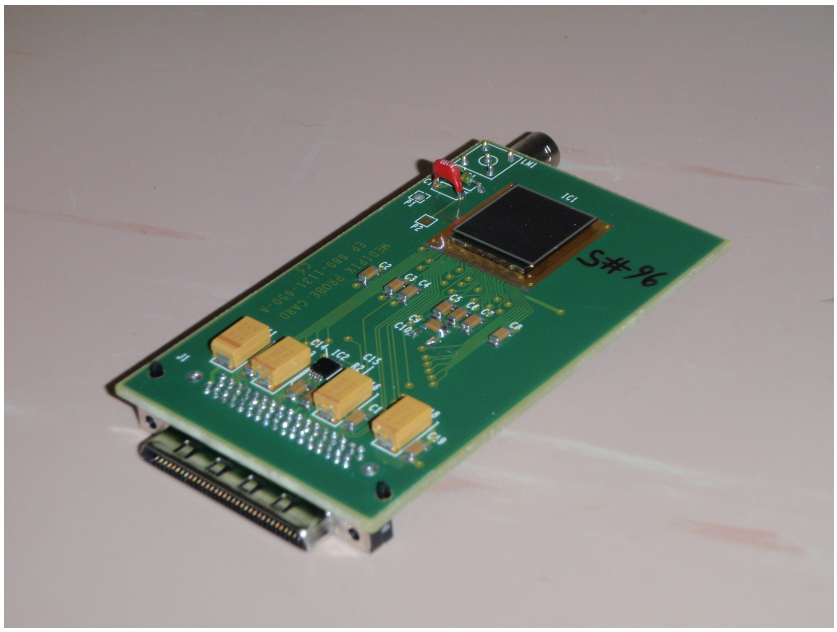

Figure 2.2: Photo of a Medipix-2 detector

To use this technology in the international linear collider (EUDET), 'Timepix', a modification of the Medipix-2 chip was created. Each pixel can be operated in four different modes. In addition to the two modes already implemented in Medipix 2 and MXR (pixel deactivated or counting whenever a signal is in a specified energy window), now 'time over threshold' and 'arrival time' can be selected. The first mode allows counting the time that the incoming signal is above the threshold. In 'arrival time mode', the time is counted from the first detection of a hit in the pixel till the end of the shutter [Llopart et al., 2007]. Within the Medipix-3 collaboration the next generation of the chip has been designed and is currently being tested. It will

enable several new modes of operation [Ballabriga et al., 2006]. To target the effect of charge-sharing, inter-pixel communication on an event-by-event base is possible in the 'charge summing mode'. Charges will be collected over a four times bigger area and pixels communicate with their neighbours to allocate the total charge to the pixel with the biggest contribution. This is especially necessary for high-Z sensor materials such as GaAs, where fluorescence photons have a mean free path length of the order of the pixel size. For high-flux applications, it is possible to continuously read from the chip at the cost of reducing the number of thresholds by half. While one counter is counting, the other one is read out. Furthermore, the 'spectroscopic mode' enables one to have eight counters and thresholds per pixel (four if the continuous readout mode is used) by binning four pixels to one superpixel of $110 \times 110\,\mu\mathrm{m}^2$. This is done during the process of bump-bonding and via a software switch. It will allow the simultaneous counting of photons in eight different energy bins per pixel each with similar noise characteristics. For Medipix-3, only a lower threshold will be used, as each threshold will have its own 15 bit counter. In order to achieve an energy window, counts can be subtracted.

In the work described in this thesis, a MXR version of the Medipix-2 chip has been used.

Detector operating mode

Photons traversing through the sensor interact with the semiconductor material producing secondary electrons. These lose their energy colliding with atomic shell electrons which creates electron-hole pairs or scattering leading to 'Bremsstrahlung'. It has been shown that the emittance of radiation from secondary electrons can be neglected for energies used in clinical diagnosis [Ewald, 2007]. As a result, the number of electron-hole pairs is proportional to the energy of the incoming photons. A 'bias voltage' is applied across the sensor which separates electrons from holes which drift towards an electrode. On their way, they induce charges that are collected in the semiconductor layer which is connected via bump-bonds to the chip. It consists of an analog and a digital part as shown in figure 2.3.

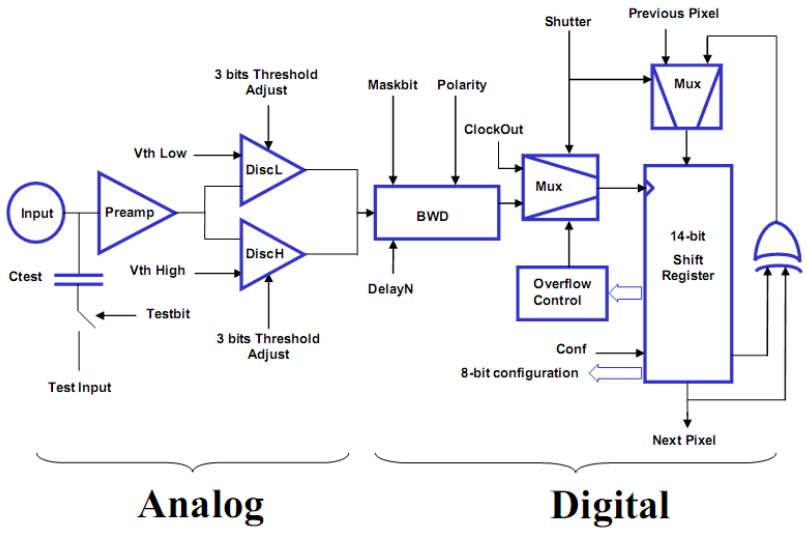

Figure 2.3: Schematics of the MXR electronics [Llopart, 2006]

In the analog part of the chip board, the incoming signal passes through a pre-amplifier where it is amplified and converted to a measurable voltage. This voltage is then processed in a discriminator which compares the pulse height of the signal to a lower threshold voltage Vth Low. At this stage, the incoming signal is modified by the 3 bit THL adjustment value and the mask bit. While the mask bit is used to switch off individual pixels that are not working properly, the THL adjustment gives an ability to adjust inter-pixel variations. Its value is calculated during the THL equalisation procedure described later in this section. If the event is found to be above the lower energy range after the THL correction, a 13 bit counter in the digital part of the chip board is incremented in this pixel. It is this possibility of comparing the collected charge to a common threshold between each chip that enables energy-selective imaging.

It is also possible to set a high threshold voltage Vth High which is used in a second, identical discriminator to give an energy window. The signal of both discriminators is then evaluated in the 'basic window discrimination' (BWD). However, in most of our measurements, this has been deactivated. Thereby we only had to adjust the low threshold. In order to measure a

spectrum, we detected the total counts in all pixels while increasing the lower energy threshold. They continuously decrease as less photons contribute. Differentiating the registered path of the curve gives a measure for the contribution of each THL step which is the spectrum we aimed to find.

THL equalisation

To correct for inter-pixel variations of the preamplifier gain, a 3 bit correction value is used for each pixel. The matrix of integers between 0 and 7 for all pixels of the chip is called a 'THL equalisation mask'. The procedure of THL equalisations is performed within the software 'Pixelman'. It consists of two steps: Setting the global THS value which defines the influence of the THL adjustment bits and finding the values for the THL equalisation mask. To create the mask, a common signal for all pixels is needed. It is possible to use an external test pulse, the edge of the electronic noise or an external gamma source. It has been shown, that using the electronic noise in the semiconductor layer of the chip board leads to a good quality threshold mask [Karg, 2006].

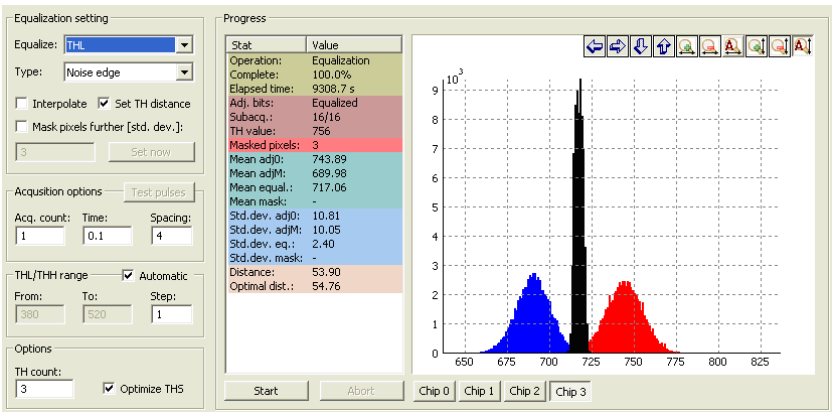

Figure 2.4: Screenshot of the software 'Pixelman' while creating the THL equalisation mask.

Firstly, a THL equalisation mask of the lowest value (0) is loaded. The number of counting pixels is registered while scanning the lower threshold value Vth Low between values corresponding to energies around 4-5 keV.

This is where the noise floor is typically expected. Plotting the derivative of the number of counting pixels versus Vth Low gives a distribution that can be seen in the blue (left) area in figure 2.4. This is the spectral response that we would get for an unequalised chip - some pixels start counting at a THL value of 675, others at 720. Now, the same procedure is repeated with a mask of the highest value (7) loaded which gives the red (right) area in figure 2.4. This time, the whole distribution is shifted. We aim for an equalised chip where all pixels start to count at the same or at least at a similar energy. The result of the equalisation can be seen from the scan with the equalised chip which is shown in the black (central) area in the same figure. All pixels start counting at a THL value of 717 ± 5 where ± 5 THL values correspond to an energy spread of about $\pm 0.75\, keV$ (see below for explanation on the energy calibration).

To find the optimal THL adjustment value for each pixel, we first have to specify the influence of the correction by the THL adjustment bit. It is defined by the global DAC value THS which has to be chosen in such a way, that the overlapping region between the red (right) and the blue (left) curve in figure 2.4 cover 1/8 of the total spacing between both curves. Thus, the full range of the 8 different values of the THL adjustment bit can be used. Once an optimal THS value has been found, the adjustment value for each pixel can be selected. To minimize the influence from neighbouring pixels, it is possible to perform the equalisation in several subacquisitions while only activating some pixels.

In our case, we choose a spacing of '4', so we performed 16 consecutive acquisitions with all but every fourth pixel in each direction masked off during the acquisition. It is possible to improve the spectral accuracy of the chip by masking pixels that are at the far end of the distribution, at the cost of losing information from those pixels. In the software 'Pixelman', further pixels can be manually added to this noisemask. Future versions of the Medipix detector are planned to have a 4 bit adjustment allowing for an even more precise THL equalisation.

Energy calibration

In order to convert THL values to energy, we identified known points from different spectra. It is possible to measure the photo-electric peak of gamma emitters, but only a few suitable radionuclides are available in the energy range between 5 and 100 keV with a reasonable half-life and availability. A second possibility is to use the monoenergetic fluorescence radiation of metal foils when irradiated by an x-ray source. The ($k\alpha_1$) peak of molybdenum is at an energy of 17.48 keV and of gadolinium at 43 keV.

These measurements can only be performed outside the scanner as the primary beam needs to be blocked. However, it is possible to identify the k-edge of these materials when measuring the transmitted spectrum of thin metal foils inside the scanner setup. The k-edge of molybdenum occurs at 20.00 keV and of gadolinium at 50.23 keV respectively. For energies above the k-edge, the excitation of electrons of the k-shell is possible which enables a further channel of interaction and changes the absorption coefficient. This leads to a drop in the intensity. This method allows a fast calibration of the system without the need for an extensive setup or radioactive sources. In future, an energy calibration phantom could be constructed with several thin metal foils which could be used to repeat the energy calibration at any time.

For calibration of the single Medipix chip in MARS-1, we identified the photoelectric peak of ^{241}Am at 59.6 keV, the k-edge of gadolinium and molybdenum from measurements of thin metal foils in transmission. In the MARS-2 setup, with the quad version of the Medipix chip, the idea of using fluorescence radiation from metal foils was tested and each chip was calibrated individually. The finite energy resolution of the THL equalisation and the fact that charges can be shared between neighbouring pixels leads to a spread of the ideally sharp spectrum. From measurements with ^{241}Am, the full-width of the distribution at half-maximum (FWHM) was estimated to be approximately 2 keV.

Both THL equalisation and energy calibration have to be repeated if the bias voltage is changed.

2.2 MARS-1

The previous section described the Medipix technology in detail. Our goal is to evaluate its use in medical imaging. To fully explore the potential of this new detector, it was for several reasons necessary to construct a CT scanner. Materials that are overlapping in a plain radiograph are separated in a CT crossectional image or 'slice'. The major imaging modality for most medical diagnosis is an x-ray CT system. Additionally, most of the published benefits for dual-energy radiography are available for CT imaging. Most of the application areas of dual-energy imaging are also suitable for our multi-energy detection system. Last but not least, the costs for CT systems are much higher than for radiographic imaging systems, hence the costs of the detector component can be higher. Due to all these reasons, the feasibility study focused on a CT scanner. As the Medipix chip gives spatial and energy resolution at the same time, the system was dubbed 'Medipix All Resolution System' (MARS). The first version of the spectroscopic CT scanner 'MARS' was constructed in 2007 in a joint effort of researchers at Canterbury University and the Canterbury District Health Board. A drawing of the scanner setup is shown in figure 2.5.

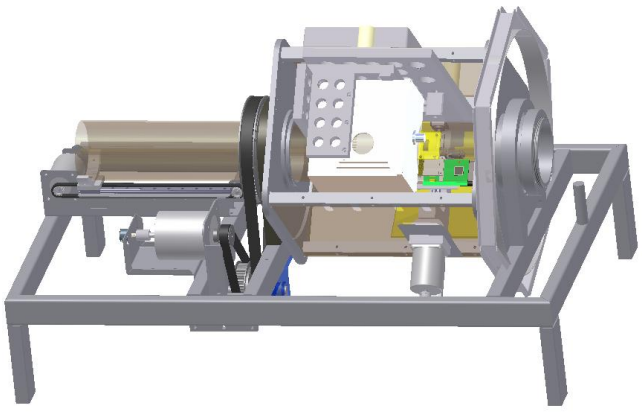

Figure 2.5: Schematic drawing of the first version of our CT scanner (MARS-1) built in late 2007.

Initial tests imaging the head of a mouse proved the correct running of

the setup. A volume rendering of voxels of the density of bone has been produced together with researchers from Ghent University (developers of the reconstruction software 'Octopus') and can be seen in figure 2.6. The sec-

Figure 2.6: Volume rendering of a mouse skull and paws from data obtained by grouping voxels of the density of bone.

ond period of measurements started in February 2008 when Markus Firsching (University of Erlangen-Nuernberg) visited our group to acquire data to test the material reconstruction algorithm he developed [Firsching et al., 2007]. Due to software problems with the scanner control interface, only one good dataset could be produced named 'mouse-2'. It has been used to develop the image enhancement techniques described in chapter 3.

Following the problems discovered during this measurement period, the scanner was upgraded as described in section 2.3.

2.2.1 General configuration

The scanner combines a micro focus x-ray tube with the Medipix-2 detector both assembled on a gantry rotating 360 degrees around the sample axis. A sketch including the notation of all axes can be found in figure 2.7.

The rotation is performed by a stepper motor in increments of approximately 0.05 degrees. Apart from the rotation, it is also possible to move the sensor along the detector translation axis. This is necessary as the sensor

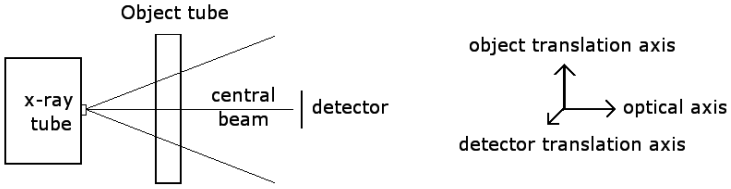

Figure 2.7: Scanner configuration and notation of the axes.

area of 14 mm × 14 mm is too small for imaging samples of typically 25 mm diameter. In addition, positioning of the sample in the direction of the object translation axis is possible. A photograph of the whole setup can be seen in figure 2.8.

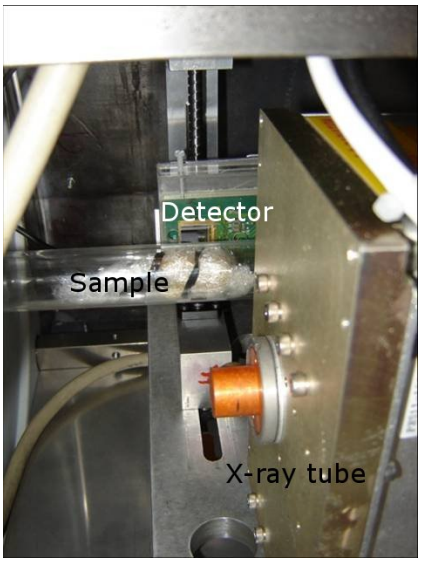

Figure 2.8: Photograph of the interior of the scanner 'MARS-1' with detector, sample and x-ray tube labelled.

The distance between the focal spot and the object (FOD) was measured to be 80 mm, the focus-detector distance (FDD) was 120 mm. Therefore, the

magnification factor, which is defined as

$$m = FDD/FOD$$

is given as $m = 1.5$. The x-ray tube can be manually moved in direction of the optical axis in order to change the magnification factor while ensuring that the whole object is covered by the emitted beam. Changing the x-ray tube location also affects the amount of translation required for the sensor.

2.2.2 X-ray tube

A Kevex THERMO PXS11-150-75 x-ray tube with a maximal voltage of 75 kV and a fixed focal spot of 45 μm was used. The tube can be operated at a maximum anode current of 0.150 mA but for longer CT scans with MARS-1, the current was limited to 0.080 mA to prevent heat damage. The target is made of tungsten and x-rays are emitted in a 34×49 degree angle through a 127 μm thick beryllium window. For most of the scans, the beam was filtered by 0.7 mm aluminium, as low energy photons mainly contribute to scattering in the sample and would not increase the flux in the detector. The spectrum of the tube has been simulated using the software srs-78 spectrum processor [Birch et al., 1979]. Input parameters were the tube target material (W), tube voltage of 75 V and the voltage ripple which was chosen to be 0 %. On request, the manufacturer gave out information on the anode angle, which is the angle of the target surface with respect to the central ray of the incoming electrons. For our tube model, this is approximately 20 degrees. Furthermore, it was specified that the beam was filtered by 0.7 mm aluminium. The resulting spectrum was adapted to the x-ray tube current and the geometry in the scanner (detector size and focus-detector distance (FDD)). It can be seen in figure 2.9.

In order to evaluate the suitability of this tube, we estimated the influence from the focal spot size on the image quality and measured the spatial distribution of the flux emitted by the tube. The modulation transfer function (MTF) gives a measure for the resolution of the system. The influence of the focal spot size $\Delta f = 45\,\mu$m and the pixel pitch $\Delta d = 55\,\mu$m on the

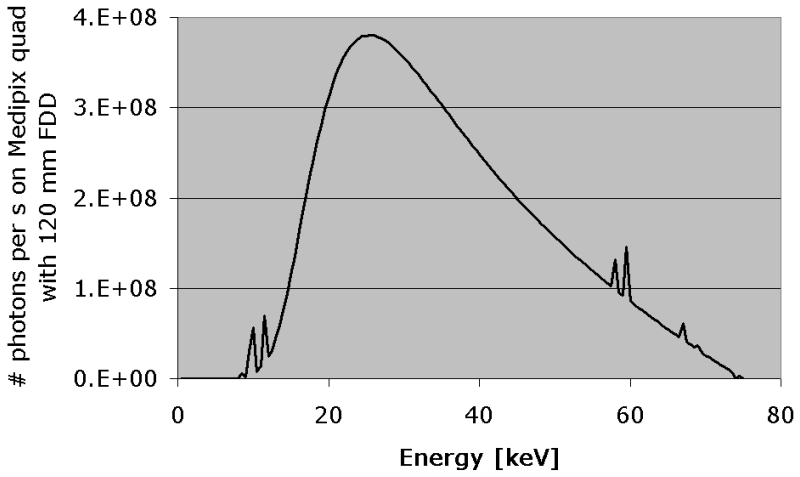

Figure 2.9: Simulated spectrum for the Kevex-Thermo PXS11-150-75 with 0.7mm Aluminum filtration at full power.

MTF is given by the following equation [Doessel, 2000]

$$MTF(\omega)_{Beam} = \left|\frac{\sin(\omega\pi\Delta f \cdot (1-1/m))}{\pi\Delta f \cdot (1-1/m)\omega}\right| \cdot \left|\frac{\sin(\omega\pi\Delta d/m)}{\pi\Delta d/m\omega}\right|$$

where ω is the spatial frequency and m is the magnification factor. The subscript MTF_{Beam} indicates that there are also other contributions besides the beam to the total MTF, such as the convolution kernel used in the reconstruction algorithm, that are not discussed in detail here. To optimise the MTF, both $d_F = \Delta f(1-1/m)$ and $d_D = \Delta d/m$ have to be minimized at the same time. Thus the focal spot size of 45 μm starts to become the limiting factor for $m \geq 2.2$. Conclusively the focal spot size is well suited for our application range. The profile of the tube was measured at Christchurch hospital using an imaging plate that could be digitally read out. A plot of the greyscale values along a horizontal and vertical path through the image can be seen in figure 2.10. The profile has been measured at a distance of 300 mm, but the scale in the plots has been converted to the geometry in the scanner (focus-detector distance of 120 mm).

The peak in the centre of the horizontal plot can be ignored as it is caused

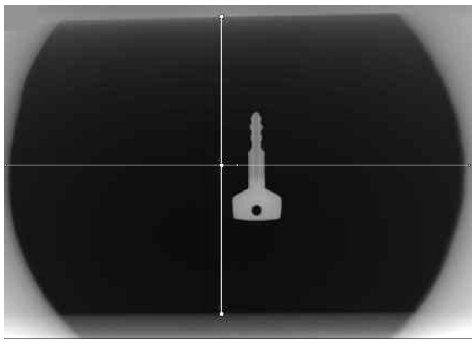

(a) Thermo Kevex PSX11-150-75 tube profile

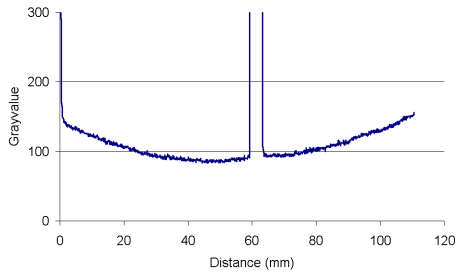

(b) plot of the greyscale values along the horizontal line (left to right)

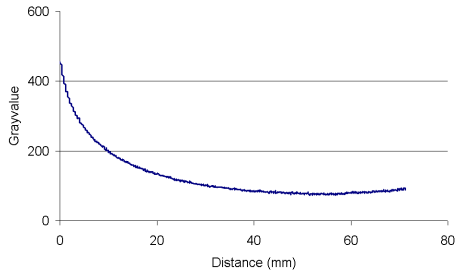

(c) plot of the greyscale values along the vertical line (top to bottom)

Figure 2.10: MARS-1 x-ray tube profile showing the gradients in intensity along the vertical and horizontal direction.

by the absorption of the metal key that has been used to give a reference point and orientation. The intensity slightly decreases towards the left and right side of the image. Along the vertical direction, the intensity of the radiation decreases noticeably towards the top of the image. This can be

explained by the 'heel effect'. It results from the absorption of x-rays in the anode material itself. This reduces especially the lower-energy photons and therefore leads to a partial hardening of the x-ray beam.

The tube has been installed in such a way that the sensor translation is performed along the central part of the horizontal path. Typical travelling ranges were 42 mm while using a single chip or 85 mm with a quad version of the chip. In this area, there is a few percent variation in the intensity. In vertical direction with a sensor width of 14.08 mm (single) and 28.38 mm in the quad version especially, there is some influence from the 'heel effect', resulting in a flux and spectral gradient along the width of the detector. This could not be avoided as it is necessary for the cone beam reconstruction to have the central line of the detector in the middle plane of the cone. To some extent, these inhomogeneities are corrected by the flatfield corrections described in section 3.3.

2.2.3 Sample tube

The sample is housed in a Perspex tube with a maximal diameter of 80 mm, however, most samples used to date fit in a tube of 25 mm inner diameter. Most biological samples that we are interested in are wet and flexible and can not be rotated. Therefore, housing the sample in a Perspex tube and rotating the x-ray tube and sensor around it is essential. Furthermore, it is possible to access the sample with supply of gas for cooling pathology samples or air flow for anaesthetised samples; this will be implemented in future versions of the scanner. The position of the Perspex tube can be moved via a stepper motor in increments of 75 μm along the sample translation axis to select the scanning area.

2.2.4 Sensor

The first version of the scanner uses a single Medipix-2 MXR chipboard bump-bonded onto a 0.3 mm Silicon sensor layer. It consists of 256×256 pixels each of a size of $55 \times 55\,\mu\text{m}^2$. It was rated after production with the highest quality grade 'A', has only few dead or hot pixels and is therefore well suited for imaging purposes.

Movement

To increase the field of view, the detector can be translated along the detector translation axis with a step size of 12.5 μm. In this configuration, 22 steps correspond to a movement of five pixels. A microstepper motor drives a gear wheel which moves the detector mount by 10 mm per full rotation. For position referencing, a 10-turn potentiometer has been used, that reports a starting position when initialized. The 10 turns of the pot and the 10 mm/turn gear limit the movement of the sensor to 100 mm.

Communication

The readout interface 'Muros 2.0' that was developed by the Medipix team at Nikhef[1], Netherlands is used to communicate with the chip and to supply the voltages necessary to operate the Medipix chip. It is interfaced via a 32 bit PCI data acquisition card (NI PCI-6533) and controlled via the readout software 'Pixelman' that was developed by the Medipix team at the Czech Technical University in Prague [Holy et al., 2006].

2.2.5 Scanner operation

The communication with the three motors is performed by a microcontroller that is interfaced via Matlab. Our group has also written libraries to control most of the functionality of 'Pixelman' from within Matlab. This includes setting all DAC values, loading a THL equalisation mask and the noisemask and performing the acquisition. The noisemask is used to deactivate individual irregular pixels.

A CT scan procedure has been automated and the parameters are defined at the beginning of each scan. They include the number of rotational steps, the number of sensor positions to enlarge the field of view, the different threshold settings and their acquisition time. A summary of typical values are given in table 3.1. At each rotational position, the sensor is first moved to its top position. Images are acquired in the specified energy bins, then the

[1] 'Nationaal Instituut voor Kernfysica en Hoge-Energiefysica' (National Institute for Nuclear and High energy physics) now called 'National institute for subatomic physics'

sensor is translated by $256 \times 55\,\mu\text{m} = 14.08\,\text{mm}$. At the new position, the acquisition is repeated. Once, the complete area has been imaged, the sensor is returned to its top position and the gantry is rotated to the next angular position. The amount of rotation between each angular position is defined at the beginning of each scan. A list of whole numbers is calculated that includes repeated corrections so that the total number of steps corresponds to a 360 degrees rotation. The image from each rotational position is called a 'projection'. Each projection is stored as a Matlab file including the scan parameters and scanner calibration values.

2.3 Upgrade of the scanner to MARS-2

The scanner is designed to be highly modular. Initial measurements of phantoms and different biological samples provided feedback for hardware and software improvements. The main targets were stability, faster scan time, methods of correcting fluctuations and improvement in accuracy. A photograph of the MARS-2 configuration is shown in figure 2.11.

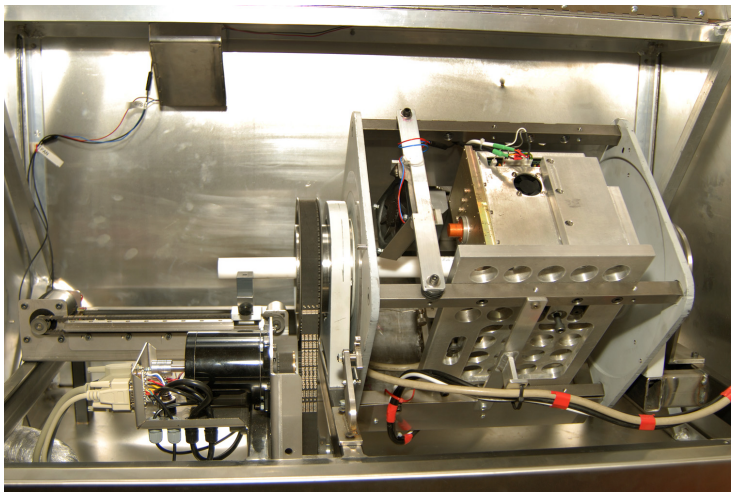

Figure 2.11: Photograph of the scanner configuration 'MARS-2' with a white scattering rod as an object and the gantry rotating around it. The x-ray tube and its cooling fan are visible at the top of the gantry.

2.3.1 X-ray tube

Cooling

To operate the x-ray tube at full power, a fan has been installed providing a continuous air flow. It was mounted using rubber buffers as vibration absorbers.

Shielding

In order to operate the scanner according to the regulations of the National Radiation Laboratory (NRL), the scanner is housed in a lead shielded box, which consists of 1.8 mm lead sandwiched between 0.5 mm aluminium and 0.5 mm stainless steel. All doors are interlocked and cable entries as well as the ventilation opening have shielded ports. A light indicates that x-rays are produced, which is interlocked to disable the x-ray controller in case of a bulb failure. A radiation survey has been performed with the result of no measurable radiation above background.

Collimator

The opening angle of the x-ray tube is much wider than the detector area. To reduce the amount of scattered radiation, we installed a lead collimator at the exit window of the x-ray tube. Furthermore, thin metal slabs of aluminium can be attached to the collimator that cover the whole beam. They filter the low energy part of the emitted spectrum and thus reduce the dose and scattering.

2.3.2 Sample tube

Bending

Bending of the sample tube occurred during our first scan. This had no effect on the CT reconstruction but limited the field of view and should therefore be avoided. Installing a new support which shortens the distance between the sample mounting points should reduce this effect.

Inconsistency between 0 and 360 degrees

Our first measurements showed that after a 2-hour scan of 360 degrees, the position of the sample had noticeably changed, which had affected some regions more than others. Reasons could be postmortem movement or relaxation of the sample, which would also explain why the movement seems to differ between two regions. To prevent this in further scans, samples were prepared and enclosed in resin. A second error that we found was a read-out cable from the chip that was not clamped correctly. This could have pulled on the chip during the rotation thus changing its position. The design review lead to an optimised cable management with a minimal force on the chip readout cable. Cables from the rotating gantry are now arranged to accommodate a half twist as they leave the scanner through a port in line with the centre of rotation. In addition, webcams are planned to be installed to monitor the scan.

2.3.3 Sensor

Quad detector

The single Medipix detector was replaced by a quad detector of four individual Medipix chips on a chip carrier board that has been developed at Nikhef. This allows imaging a two times wider area while reducing the scan time, as only two translation stops (instead of 3 stops) are necessary to scan a 25mm object.

The layout of the quad detector is shown in figure 2.12. It has a sensitive area of $28.38\,mm \times 28.38\,mm$. However, edging pixels have a three times bigger area of $55\,\mu$m $\times 165\,\mu$m and the four central pixels are nine times bigger than a standard pixel. Methods for handling this are discussed in section 3.2.2.

The timer settings for the acquisition have to be chosen cautiously to prevent saturation in the bigger pixels. Mostly, this cannot be achieved for the four $165\,\mu\text{m} \times 165\,\mu$m big super-pixels in the middle of the sensor making them insensitive.

Furthermore, each of the four chips has an individual energy response. Energy calibration measurements led to an equation for each chip to convert

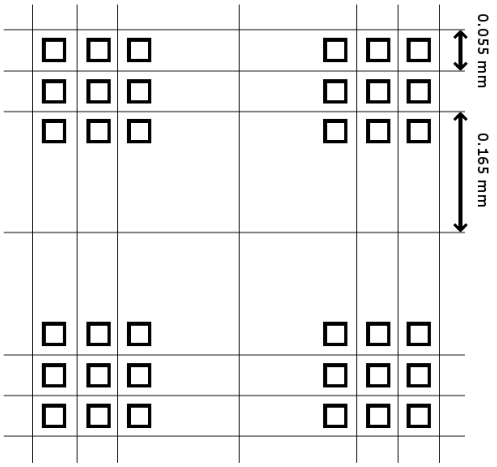

Figure 2.12: Layout of the quad detector indicating the bigger edging pixels.

from THL settings to energies. For each scan, the desired energies for the lower thresholds were chosen, converted in THL values for each chip and set during the acquisition.

Skew adjustment

In our first measurements, the detector was skewed from vertical by approximately 0.5 degrees, leading to an offset of two pixels at the edge between different detector positions. We constructed a new detector mount with a micrometer screw to correct for this skew of the chip carrier board. By imaging a vertical wire, careful realignment between different detector positions is now possible.

Reducing fluctuations

The evaluation of our first data showed that the number of counted photons changed with each detector position. This could be due to tube fluctuations or timer settings. As the timer settings are sensitive to the read-out

board voltage, the initial power supply was tested and showed a ripple of ±20%. It was replaced by a stabilised voltage supply. Remaining fluctuations are corrected by introducing an overlapping area between the detector stops and a flatfield-ROI that is never covered by the object during the rotation. The method for the normalisation is described in more detail in Section 3.5. Eventually, the readout interface has been replaced with an improved version ('Muros 2.1'). Furthermore, a new readout command now reports the actual acquisition time which enables the individual correction of each chip in case it deviates from the timer setting.

Longer travel range

To achieve a longer range of travel for the sensor, the limiting 10-turn potentiometer was replaced by a contact sensor. It defines the starting point of the motor during its initialisation and is mechanically accurate in the order of a few μm. In the current MARS-2 setup, the new travel range is 106.25 mm. Now the C-arm supporting the sensor motion is the limiting factor.

2.3.4 Scan mode

To improve the accuracy of the scan, the movement of the sensor and the rotation were performed with a whole number of steps. For the new quad chip ($28.38 \times 28.38\,\mathrm{mm}^2$) this meant implementing an overlapping area of six pixels between each detector position which results in a movement of 2244 steps. The number of angular positions was chosen to be a fraction of the total numbers of steps that cover 360 degrees. To increase the speed of the acquisition, new scan modes were implemented. One idea was to alternate the direction of the sensor movement between each projection. Such a scan type is likely to be influenced by backlash of the sensor translation screw. This was tested by repeatedly moving the sensor in one angular position. It was found that the deviation between each acquisition was in the order of sub-pixels, even for a large number of movements. With the current scan version, the movement of the sensor is most accurate but slow. Therefore, scanning one full rotation in one sensor position and then moving to the next position can speed up the scan. This mode has now become the standard

operating procedure.

2.3.5 Software

One of the biggest problems of the MARS-1 setup was the instability in the control software resulting in unpredictable crashes. It was found that the interface between Matlab and the readout software 'Pixelman' caused those problems. Hence it was replaced with a new library which contains only the necessary routines. This finally led to a stable scanner software.

2.4 Ideas for next version MARS-3

In addition to upgrading the scanner to the version 'Mars-2', the design of the successor 'MARS-3' was planned. The December 2008 version of the design drawings can be seen in figure 2.13.

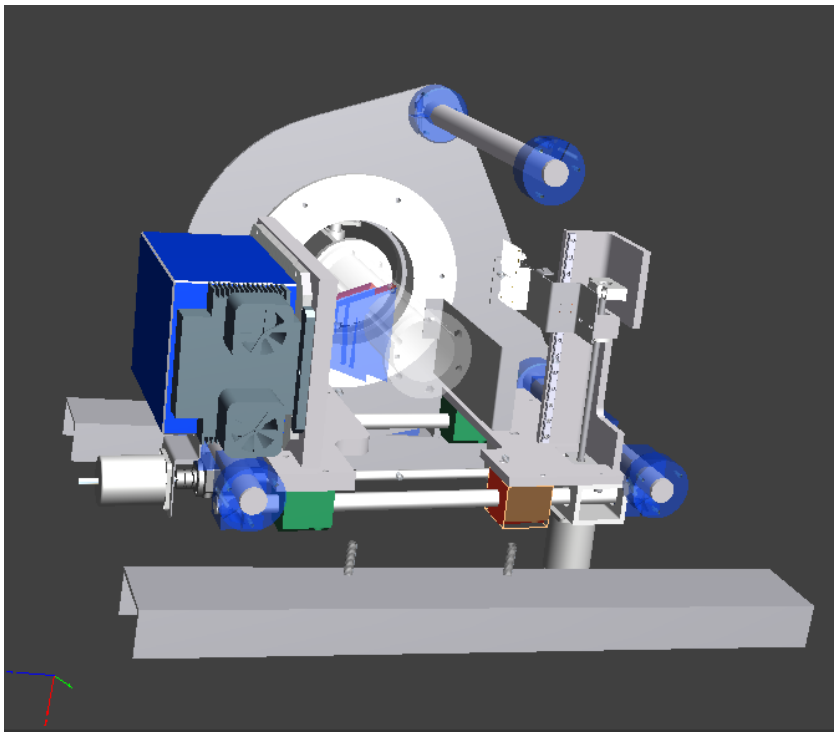

Figure 2.13: Design of MARS-3 scanner as at December 2008.

2.4.1 X-ray tube

As an x-ray tube, the model 'SB-80-1k' from SourceRay has been selected. Its maximal current is 1 mA at 80 kV with a focal spot size below 50 μm. Therefore it is comparable to the MARS-2 model but allows an 8 times higher flux. It has an inherent filtration of 1.8 mm Al, the resulting spectrum is shown in figure 2.14, using the srs-78 spectrum processor [Birch et al., 1979].

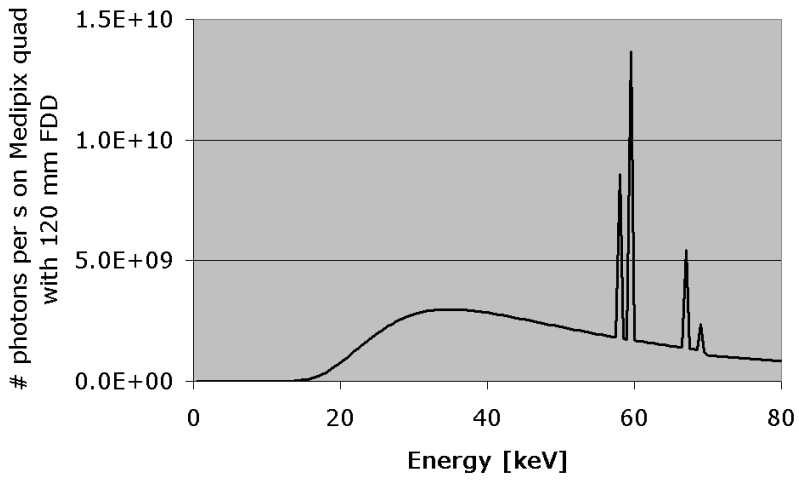

Figure 2.14: Simulated spectrum of the SB-80-1k x-ray tube at full power with inherent filtration of 1.8mm Al.

Furthermore, this model has a reported rise time of 250 ms allowing to shutter off the tube while moving to reduce the applied dose. The measured tube profile can be seen in figure 2.15.

It shows similar characteristics than the Kevex tube that is currently in use. With a weight of 6.35 kg and a 40 degree beam angle, it can be easily implemented into the new design. Stress analysis of the model with 20 kg on each side of the gantry using the finite element modelling tool embedded in 'Autodesk Inventor Professional 2008' showed bending of the gantry in orders of $\pm 20\,\mu$m.

2.4.2 Sample tube

A new sample tube will be used in MARS-3. It will be accessible with designated channels for supply of cooling gas and air from one side. Furthermore, it will be possible to load the sample tube inside the scanner setup where it clicks into the holder.

2.4.3 Sensor mounting

Medipix chipboards come in different shapes and sizes. To be able to include future versions in the MARS-3 scanner, the detector mount is designed in such a way that the board is supported from the side and there is free space behind the detector. This design allows for a range of sensor boards, for example the Ethernet based readout system that is currently under developement in Nikhef.

2.4.4 Motor driven selection of the magnification

In the new scanner setup, both the x-ray tube and the sensor mount can be translated along the optical axis via motors. This allows an easy change to the magnification factor for each acquisition. A procedure could be automated that allows the determination of the ideal magnification factor by measuring the centre of rotation and the bending of the tube. It could also be possible to determine the size of the sample tube from an acquisition with known magnification factor and position of the x-ray tube and sensor mount.

2.5 Discussion

Challenges of the current setup are for example the dead rows and columns in the quad detector. The new quad detector setup currently under developement at Nikhef called 'High REsolution Large Area X-ray Detector' (RELAXD)[2] targets this issue. It incorporates an additional pitch adaption layer so that the sensor material covers the whole area of the chip. An alternative could be an array of single detectors that is shifted once. The sensor layer

[2] http://www.nikhef.nl/pub/experiments/medipix/relaxd.html

silicon is not ideal for medical imaging purposes due to its limited sensitivity beyond 20 keV. Additional sensor materials are being produced and tested within the collaboration and from external suppliers. We are currently investigating a CdTe chip which should show an improved performance with a detection efficiency of approximately 90 % at 50 keV. Even after the threshold equalisation procedure and the flatfield correction, pixels still show a constant pattern of 'noise' due to their individuality. A more optimised flatfield procedure could help to overcome this. It is further hoped, that with the future version of the Medipix detector with a 4-bit threshold equalisation value, the pixels can be equalised better. Evaluating the data showed that the gantry performs a spiral scan with an offset between images from 0 and 360 degrees of about 1 pixel in direction of the sample translation axis. This could be taken into account by a spiral configuration CT reconstruction. To check the alignment and orthogonality of the scanner and to find the parameters for the centre of rotation and the central line of the detector, a phantom has been constructed. Evaluation of this work is still ongoing.

2.6 Summary of Chapter 2

This chapter provided an overview of the Medipix technology and its implementation into the MARS scanner. Medipix is an energy-selective photon processing detector enabling spectroscopic imaging. Methods of how to equalise the spectral response of each pixel and how to perform an energy calibration have been implemented. Two iterations of the spectroscopic scanner 'MARS' have been successfully built, the final design of the third version is currently underway. Key components of the scanner have been upgraded in the second design version 'MARS-2' to fix bugs, make the scanner faster, more accurate and to achieve a better image quality. The next version of the scanner will allow better access to the sample, motor driven selection of the magnification factor and a detector mount that allows upgrading to future detector versions. We showed that the focal spot size of the current x-ray tube is not limiting the image quality. A new x-ray tube has been selected which shows similar parameters at an 8 times higher flux thus reducing our scan time. The work in this chapter has been presented at the IEEE Medical

Imaging Conference which took place in Dresden, Germany in October 2008. It is planned to be submitted to the 'IEEE Transactions on Nuclear Science'.

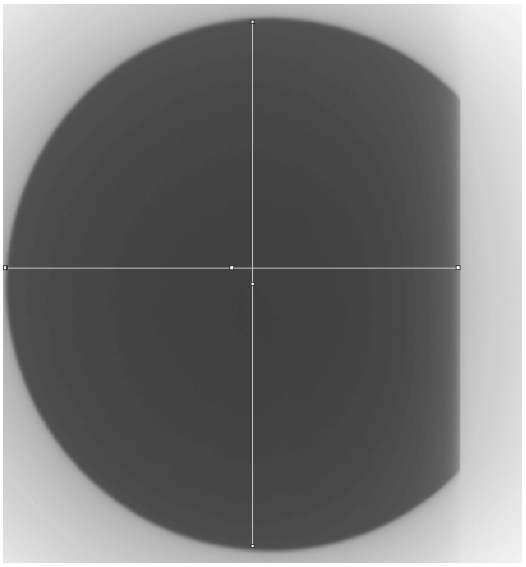

(a) Sourceray SB-80-1k tube profile

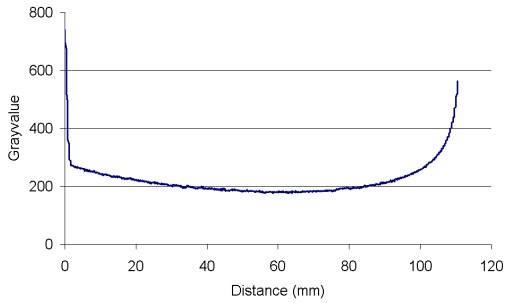

(b) plot of the greyscale values from left to right

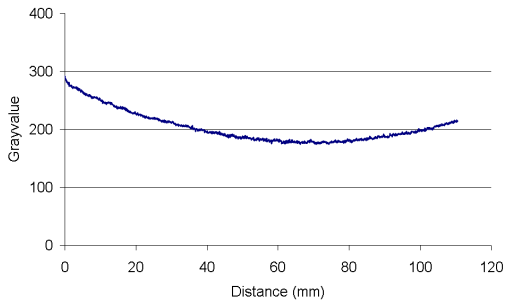

(c) plot of the greyscale values from top to bottom

Figure 2.15: MARS-3 x-ray tube profile showing intensity gradients along the vertical and horizontal direction.

Chapter III

Image correction and tomographic reconstruction

This chapter describes all processing steps that are necessary to create a tomographic reconstruction from raw data. The software package 'Octopus' was designed to allow pre-processing and tomographic reconstruction for multiple types of detectors [Dierick et al., 2003]. It allows correcting for randomly distributed noise in the dataset, fluctuations between different projections using a user defined region of interest (ROI) and to filter ring artefacts. From the software documentation, most of the parameters appear to be arbitrary. Discussions with developers of 'Octopus' in the final state of the project revealed more insight into these values. However, we wanted to gain more understanding of and influence on the pre-processing steps. Therefore, all pre-processing steps have been implemented in Matlab. This allows us to optimise the routines for the specific needs of the Medipix detector and to test and implement additional steps for our configuration.

With two different scanner configurations, different methods have to be applied. The first two sections describe datasets from the scanner configuration MARS-1 and MARS-2, respectively and specific correction routines needed for their evaluation. In the following sections, further image correction techniques are presented. For each technique, the problem is stated followed by an explanation how it is solved in the software package 'Octopus' and in the Matlab routines developed for the MARS-1 and MARS-2 configuration.

3.1 Description of the data from MARS-1

3.1.1 'mouse-2' dataset

The 'mouse-2' dataset was acquired on the 17th of March 2008 working with Markus Firsching in the scanner configuration MARS-1. The mouse sample was prepared by a team of molecular biologists of the Christchurch Cardioendocrine Research Group (CCERG), based at the Christchurch School of Medicine. The mouse, a 26.9 g male, was anaesthetized and 800 μl of iodine (50% Omnipaque, 50% sterile water) was given orally. After euthanisation, 400 μl of Magnevist (containing a 17% barium solution) was injected into the suspected heart region.

Figure 3.1: Radiograph of 'mouse-2' with a iodine solution in the gastro-intestinal and barium in the pleural space.

A radiograph obtained from an imaging plate (CR system) at Christchurch Hospital can be seen in figure 3.1. It showed that the iodine solution was located in the gastro-intestinal tract, whereas the barium has missed the heart. We then decided to scan the abdominal region with only one contrast agent, as the barium was spread in the pleural space and not localised in any specific organ. Four energy bins were chosen with the high energy bin

THH	1023	1023	1023	1023
THL	714	680	577	520
Energy [keV]	12	17	33	42
Time [sec]	0.3	0.3	1.5	3

Table 3.1: Scan parameters of the 'mouse-2' scan showing the four energy bin and timer settings.

deactivated so that energies above 12, 17, 33 and 42 keV contributed to each acquisition. Table 3.1.1 shows the scan parameters including timer settings.

The tube voltage was set to 75 kV with 0.079 mA and the beam was filtered by 0.7 mm aluminium. To enlarge the field of view, the sensor was moved to three positions for each projection, altogether 180 projections have been acquired. The total scan time was approximately three hours.

Markus Firsching applied the method of material reconstruction (MR) described in section 4.1 on the data. He chose water and iodine as base materials and sent us the resulting projections for evaluation. The dataset of both raw images and MR images is called 'mouse-2' dataset. Examples from the projections at 0 degrees for all four energy bins and the two base materials 'iodine' and 'water' can be seen in figure 3.2.

3.1.2 MR dataset specific calculations

For the material reconstructed set of images of the projected density of water and iodine, two additional calculations have to be performed to be consistend with the other projections. For faster processing, a 2×2 binning was applied during the material reconstruction which was undone as a first step by enlarging each pixel. As the matrix derived from the algorithm represents the spatial distribution of the projected partial density $p_j = \int \rho_j(x, y)dxdy$, it needs to be converted to a 'MR pseudo-radiograph' which can be done by calculating the negative exponential of each value. This leads to a set of functions of the form $f(\rho_j(x, y)) = \exp(-\int \rho_j(x, y)dxdy)$ from which the values for $\rho_j(x, y)$ can be found via an inverse Radon transformation [Radon, 1917]. The material reconstruction algorithm is described in more detail in section 4.1.

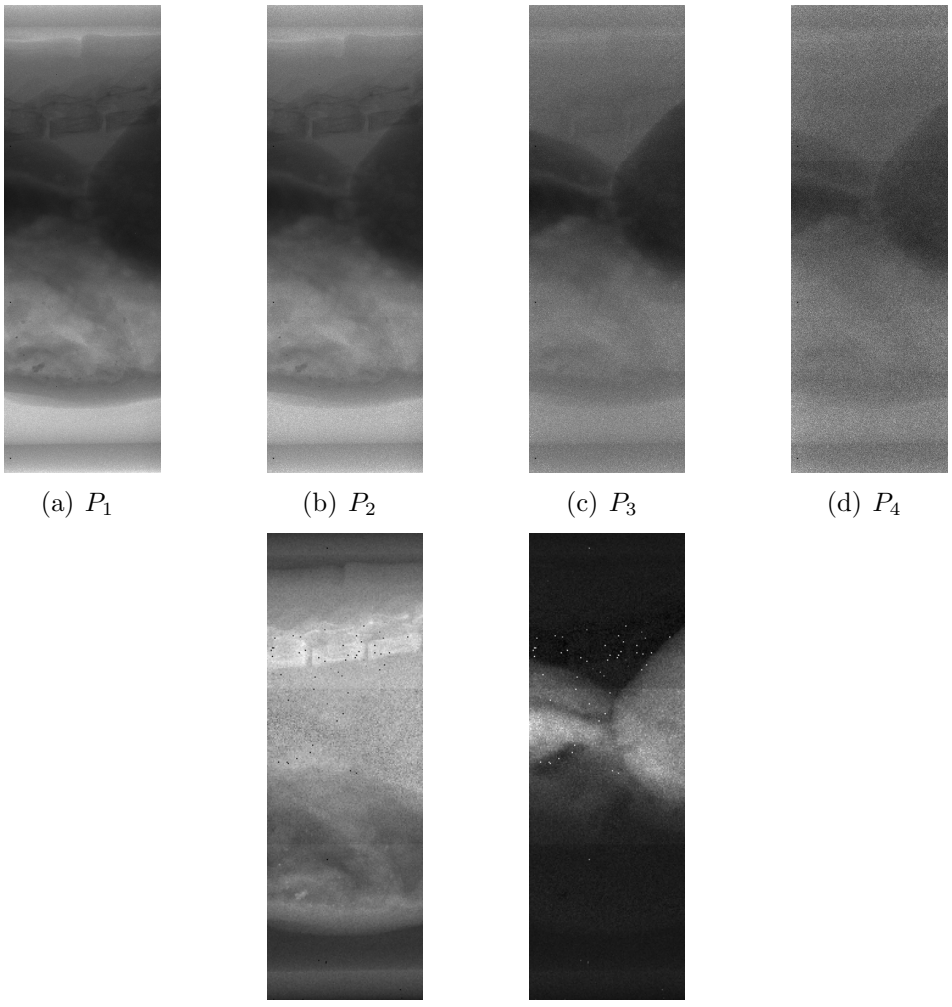

(a) P_1 (b) P_2 (c) P_3 (d) P_4

(e) W (f) I

Figure 3.2: Raw images of the 'mouse-2' dataset: Projections of the four energy bins (a) - (d) and MR images for the base materials 'water' (e) and 'iodine' (f). In images from energy bin 1 and 2, both contrast agent and spinal bone show a high contrast - in the third and fourth energy bin image, only the contrast agent is visible. MR image 'iodine' has isolated the contrast agent, MR image 'water' shows the remaining image.

3.2 Description of the data from MARS-2

3.2.1 Datasets from the MARS-2 configuration

In the MARS-2 configuration, several datasets have been acquired by our team. They focused on multi-contrast agent imaging and the use of contrast

agents to highlight e.g. the vascular system of a mouse.

As an example, on the 6th of June 2008, 'mouse-10' has been prepared with barium injected into the right heart ventricle. The contrast agent spread within the vascular system as can be seen from a plain radiograph in figure 3.3. The mouse was enclosed in resin and stored in a fridge. On the 14th of August 2008, we scanned 'mouse-10' with the low energy threshold for all four chips of the quad detector set at 10 keV, the high energy threshold was deactivated. As this was a test run during commissioning of the scanner, only one energy bin was used. The acquisition time was set to 1 second and the sensor has been moved to three sensor positions for each projection with an overlap of 6 pixels. Altogether, 263 projections have been acquired with the x-ray tube at 75 keV and 0.15 mA. The total scan time was 110 minutes.

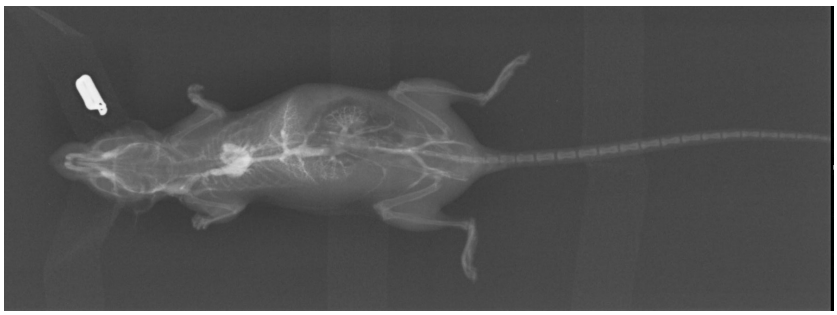

Figure 3.3: Radiograph of 'mouse-10' showing the contrast agent barium in the vascular system.

3.2.2 Quad interpolation

One of the major changes of the 'MARS-2' configuration in terms of image corrections is the fact that the single chip was replaced by a quad array of detectors. This makes it necessary to interpolate missing rows and columns. This additional step is best performed after the equalisation and noise filtering, so that pixels are already equalised.

The layout of the quad detector is shown in figure 2.12. As discussed before, two additional rows and columns need to be inserted at each edge between two chips as indicated in figure 3.4. The next step is to assign

values to these new pixels.

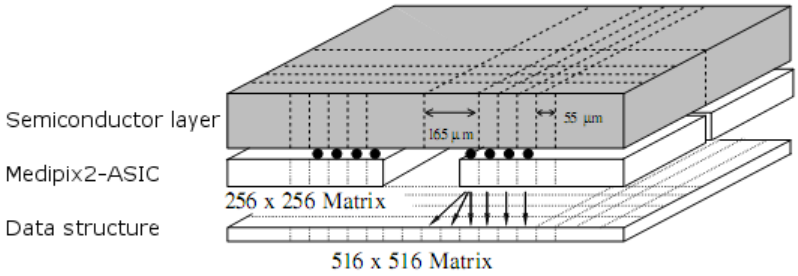

Figure 3.4: Data structure of the Medipix-2 quad. Edging rows and columns are three times bigger and additional rows and columns are inserted for each edging chip [Niederloehner, 2006].

The following method for interpolating was found to be fast and accurate enough and leads to a continuous transition. For each pair of three pixels, a third of the value is assigned to the middle pixels. A linear interpolation is performed between neighbours within one row or column respectively.

Result

The result of the interpolation can be seen in figure 3.5, where the chosen interpolation method (right) is compared to sharing the counts between the three pixels (left).

3.3 Equalisation of pixels

Integrating 2D imaging sensors such as CCD or flatpanel detectors typically show a randomly distributed noise over the whole sensor. Medipix images, on the contrary, are almost noise free. However, there are substantial variations between individual detector elements as each pixel is flip-chip bonded to an individual processing electronic circuit. These don't change between different acquisitions, but show a fixed pattern.

Thus, the whole chip can be seen as a matrix of individual spectroscopic detectors. It is necessary to equalise both, the spectral response of the pixels,

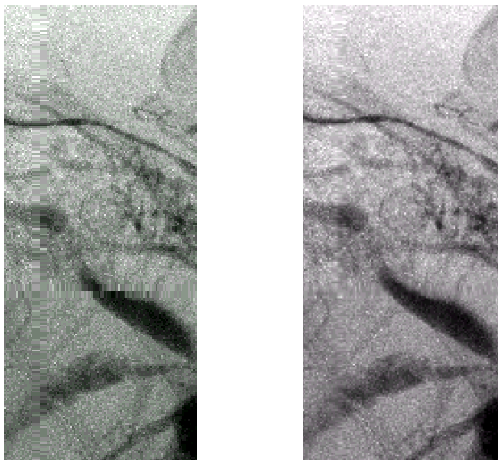

(a) Sharing the counts equally

(b) Linear interpolation

Figure 3.5: Different methods of interpolating inserted rows and columns.

and their count rate. The equalisation of the spectral performance has to be done prior to the acquisition and is described in section 2.1. The following procedure aims at correcting remaining inhomogeneities in the count rate between pixels.

3.3.1 Flatfield correction in 'Octopus' and Mars-1

To begin with, a series of 10-20 'flatfield images' were taken. These are taken with no object in the beam and with the same timer settings as the scan. As the tube profile changes dependent on the detector position, images are taken in each position. The average flatfield image is calculated and each pixel in the projection dataset is divided by its flatfield counterpart. This reduces the fluctuations between pixels to some extent.

3.3.2 Improved Flatfield correction in MARS-2

To achieve a better statistical significance, 100 images are acquired in each energy bin. Having an object in the beam significantly changes the spectrum incident on the chip. In order to simulate the absorption in the object, we placed a 30 mm thick plain Perspex slab in the open beam for the flatfield

acquisitions. This improved the flatfield corrections noticeably. It works most effectively in the central part of the image, where the approximation of the object by the Perspex slab is most appropriate.

Result of the Flatfield correction

Figure 3.6 shows the result from the equalisation of the pixels from the 'mouse-10' dataset. Only a small region of the whole image is shown. It can be seen that applying a flatfield leads to an equalisation of the pixels and reveals anatomical details. Remaining inhomogenieties can be further corrected by the ring artefact filter described later in this chapter.

3.4 Noisefilter

Some pixels are noisy which means that they always count a lot more or less than the average pixel. Others have been masked during the threshold adjustment procedure and show a value of '0'. Furthermore, it's possible that pixels are overcounting, showing the maximum possible counting value. Here, all those pixels are called 'bad pixels'. They need to be found and interpolated. The noise filtering routine needs to be applied at an early stage to prevent influence on the normalisation routines that are described in the next section.

3.4.1 Built in method in 'Octopus'

The software package 'Octopus' allows correcting for randomly distributed noise over the whole sensor area. The user can specify a threshold value t to select the influence of the filtration. Only pixels that deviate more than t times the square root of the average value of its eight surrounding neighbours are selected for interpolation. A 3×3 median filter is applied to those pixels. The threshold can be seen as a number of standard deviations from the statistics of the distributed noise. Recommended values are between 2 and 3 where a smaller value leads to a larger number of corrected pixels.

For a photon-processing detector such as Medipix, this method of finding noisy pixels is not ideal. Pixels deviate from each other caused by electronic

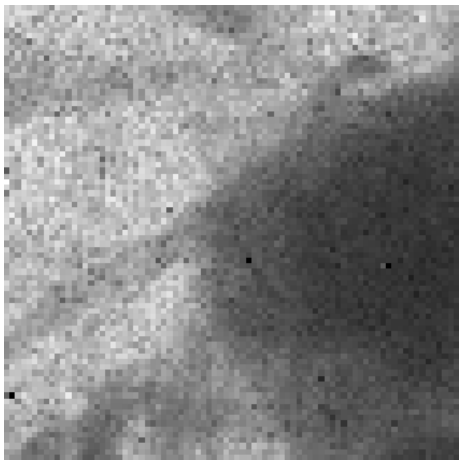

(a) Detail of original image

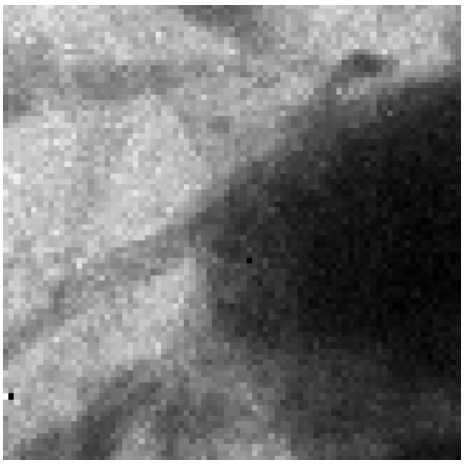

(b) Flatfield corrected image

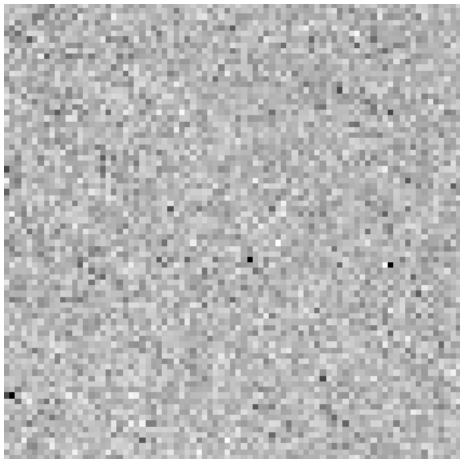

(c) Detail of flatfield image

Figure 3.6: The result of the flatfield equalisation procedure can be seen between the original (a) and processed image (b). The flatfield image used is shown in (c).

parameters and not randomly distributed Poissonian noise. They show a fixed pattern that does not change between acquisitions as opposed to the statistically fluctuating noise common in other detectors. Thus we have developed our own method.

3.4.2 Initial methods for MARS-1

A first attempt was to correct for the noise in the 'mouse-2' dataset. In the material reconstructed dataset, randomly distributed 'salt and pepper noise' has been prevalent, caused by non-converging values in the MR algorithm. Thus, it was decided to apply a median filter to the whole images in the dataset. This removes the noise and corrects also to some extent for the uneven responses of the individual pixels further.

3.4.3 Improved methods for MARS-2

In the MARS-2 configuration, the method for correcting the noise was optimised. Our equalisation method differs from the built in function from 'Octopus', as it uses flatfield images to find noisy pixels.

As a first step, noisy pixels are located. They are found by looking at the histogram of the mean flatfield acquisition of the first energy bin and demanding a 'good pixel' to be confined within 5 standard deviations σ from the mean value of all pixels. In each acquisition, masked pixels with a value of '0' and overcounting pixels with a value of '11810' are found and added to the list of 'bad pixels'. All those pixels are then interpolated in the individual acquisition by applying a median filter at their position. The median filter is a rank filter of the order 5, meaning that the grayscale value of the central pixel and its surrounding 8 pixels are put in an order of decreasing value. The fifth value is chosen and assigned to the central pixel. This avoids the influence from up to four surrounding 'bad pixels'. Instead of ranking the 8 surrounding pixels, only the 4 nearest neighbours could have been chosen and the third value could have been used for the central pixel to get a more accurate description. Nevertheless, we chose to use the bigger kernel to minimise the influence of clusters of 'bad pixels'. An example of such a cluster can be seen in figure 3.7. Correcting only 'bad pixels' rather than applying the filter to the whole image ensures that as much as possible of the original structure is preserved.

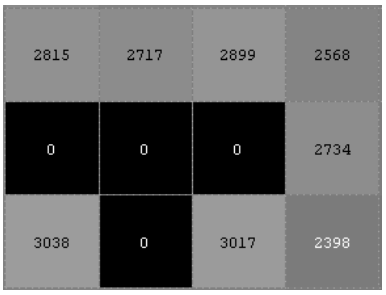

Figure 3.7: Example of an area of pixels containing four bad pixels.

Results

Different to the way 'Octopus' filtered the noise, we chose to use the flatfield data rather than the individual projections to find 'bad pixels'. This is possible due to the fixed pattern of the inter-pixel variation between acquisitions. Furthermore, we did not compare each pixel to its neighbouring value but to the mean value of the flatfield image, which shows a much better counting statistic. This technique helps to preserve most of the original structure in the image.

3.5 Flux normalisation

A variation in intensity from different positions of the detector occurred in the data of the 'mouse-2' experiment in the MARS-1 configuration. It was especially noticeable in the material reconstructed (MR) data due to enhancement by the MR algorithm. Hence, it was necessary to correct both, fluctuations between different detector positions, and between different projections.

3.5.1 Embedded function in 'Octopus'

The software package 'Octopus' was not used as it allows correcting fluctuations only between different projections using a fixed region of interest. It is not suitable for corrections between different detector positions.

3.5.2 Enhanced method for flux correction in MARS-1

For the 'mouse-2' dataset and especially the material reconstructed projections, the correction of fluctuations was essential. It was performed in two steps. Firstly, variations between different sensor positions have been corrected. In a second step, images from different projections were normalised.

Flux correction between different detector positions

In general, an overlapping area of a few pixels between two detector stops allows calculating a ratio of the intensities between both acquisitions. Multiplying each pixel in the second detector position by this ratio creates a normalised projection.

However, in the scan of the 'mouse-2' dataset, no overlap had been implemented. Therefore, to correct for fluctuations between different detector positions, we used the ratio between the mean value of edging rows. This was only possible, as biological structures don't show any sharp edges that could have influenced the procedure. For future scans, an overlapping area of a few pixels between each detector position has been implemented.

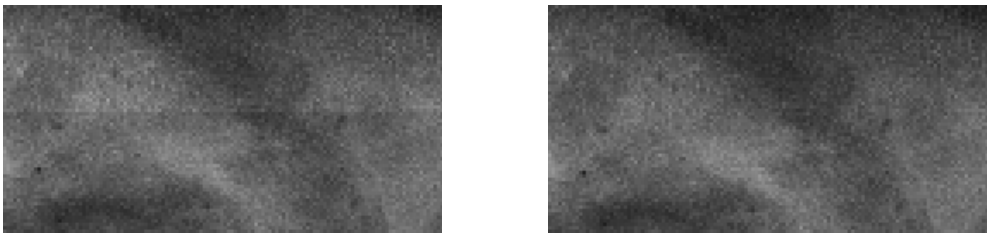

(a) (b)

Figure 3.8: Detail of image before (a) and after (b) flux normalisation between different detector stops.

In figure 3.8, the result of the normalisation of different detector positions can be seen. The left image shows the original image where the transition between two detector positions is visible. In the image on the right, the flux correction has been successfully applied, leading to a continuous transition between detector positions and no visible edge. In particular, this prevents

ring artefacts in the cone beam reconstruction which are described in section 3.7.

Correcting fluctuations between projections

After the fluctuation correction between different detector stops, fluctuations between different angular positions must be considered. To equalise the intensity fluctuations between different projections, a fixed region of interest (ROI) has to be chosen which is never covered by an object. As this was not practicable in the 'mouse-2' dataset, we used the average mean value of the whole image to obtain a measure of the intensity in each projection. Then we normalised each projection by dividing it by its mean value. The chosen method assumes rotational-invariant objects which in our case is only an approximate. For all other samples, different angles of view lead to different total counts. In our case, however, the method worked reasonably well, which can be seen when visualising the projections in a video. In the future, acquisitions will be performed with sufficient open beam in view at all times.

3.5.3 Flux normalisation in MARS-2

With an overlapping area between different detector positions and sufficient flatfield in view for all acquisitions, further flux normalisation can be performed using the ratio between the two acquisitions of the same area. However, as described in section 2.3, we've identified the power supply for the readout-board as the main source of fluctuations and replaced it thus stabilising the timer settings of the chip. This reduced the problem to an extent that for most of the experiments, no correction was needed in the MARS-2 configuration.

3.6 Ring artefact suppression

In the reconstructed CT data, ring artefacts are prevalent in some datasets. They result from the fact that individual pixels have a characteristic be-

haviour which becomes obvious when representing the data as a sinogram[1] as shown in figure 3.9. Vertical streaks are visible indicating the individuality of each pixel. The influence of this effect has been reduced by applying the flatfield correction described in section 3.3 and by removing edges between detector positions as described in section 3.5. Our aim is to further filter the ring artefacts, if necessary.

3.6.1 Solution in 'Octopus'

The exact method of the ring-artefact suppression in Octopus is kept confidential. The parameter which can be selected is a kernel size expressed in number of pixels. Typical levels are 2 or 3 for 512^3, 3 to 5 for 1024^3. A bigger kernel size means heavier filtering, but possibly introducing new artefacts.

3.6.2 Our method for the MARS-1 and MARS-2 configuration

The ring artefact correction procedure has been adopted from [Niederloehner et al., 2005]. It makes use of the whole dataset which gives a good statistical measure of each pixel's behaviour. In the following, we work on each projection individually and finally generate a new set of sinograms.

As a first step, we create a mean projection from the sum of all projection images. We then smooth the image by convoluting each pixel with a 2D Gaussian kernel. According to the Fourier convolution theorem, this can be performed as a multiplication in Fourier space [Doessel, 2000]. This second image gives us an idea how an ideally homogeneous mean projection would look like. By dividing each pixel's value of the 'mean projection' by the corresponding value in the smoothed image, we create a matrix of correction values. Finally, we multiply each pixel in our original data with its correction value and thus achieve a homogeneous response from each pixel.The result can be seen from the difference between the unprocessed (left) and processed (right) sinogram in figure 3.9. Most of the vertical streaks have been successfully removed. Remaining horizontal streaks are resulting from fluctuations

[1] Each sinogram represents one detector column seen from different angles, each column in the sinogram contains the data from one pixel.

between different projections which could not be totally eliminated by the flux normalization procedure described above.

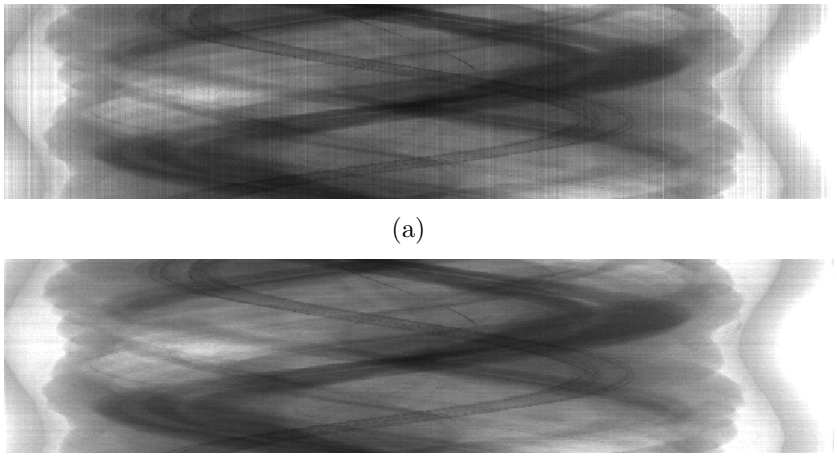

(a)

(b)

Figure 3.9: Sinogram before (a) and after (b) ringartefact filtering. Ringartefacts are caused by the vertical lines in the sinogram.

The influence of this routine on the image quality is marginal as can be seen from figure 3.10. However it is optional to apply this method.

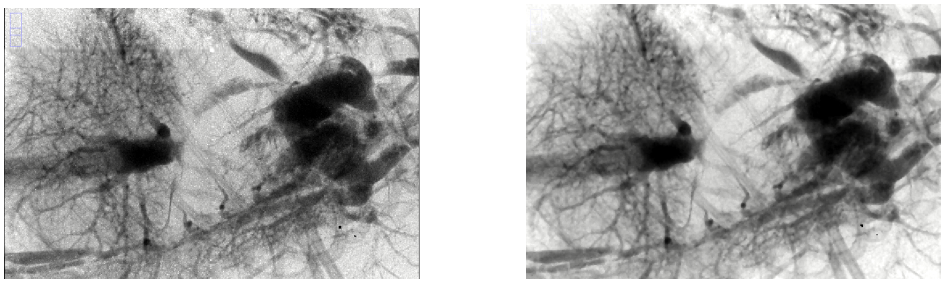

(a) (b)

Figure 3.10: Projection before (a) and after (b) ringartefact filtering showing the influence of the filter on details in the image.

3.7 CT back projection

For this final step, the 3D CT reconstruction software 'Octopus' was used. Each sinogram was converted from a matrix of float values to a 16 bit tiff image. To preserve maximal precision and cover most of the 16 bit range, a common offset value was subtracted from all matrices before multiplying them by a common gain factor. Both factors were chosen manually.

The sinograms were then loaded into 'Octopus' where several geometrical parameters have to be defined for the cone-beam reconstruction. In the MARS-1 configuration, the source-object distance was measured to be 80 mm, the distance between source and detector was 120 mm. The vertical centre where the central beam hits the detector was chosen to be at 125 pixels. As a filter kernel for the filtered back projection, a ramp filter was used.

The outer borders of the sinusoid track in the sinogram could be used to determine a rough value of the centre of rotation. It was manually adjusted from the results of the reconstruction of a single slice. As a reference point in the 'mouse-2' dataset, the shape of the spinal bone was optimised.

In the 'mouse-2' dataset, it was found that the 180th projection did not show the image after 360 degree as originally planned but after 358 degree. This was related to a bug in the scanner code that has been corrected in 'Octopus' by specifying the angle of the last image to be 358 degree.

3.8 Comparison of image correction techniques

Figure 3.11 shows the results from the CT reconstruction of 'mouse-2' in the 12 keV energy bin. The first image shows the reconstruction of the unprocessed data, where ring artefacts are dominating. For the image in the middle part, the correction methods from 'Octopus' including a ring artefact filter have been applied which improved the image quality. The last image shows the result after our processing steps described above have been applied. Structures in the image appear to be sharper and no apparent noise and artefacts are visible. It can be seen that our aim of improving the image processing done in the software 'Octopus' has been successful.

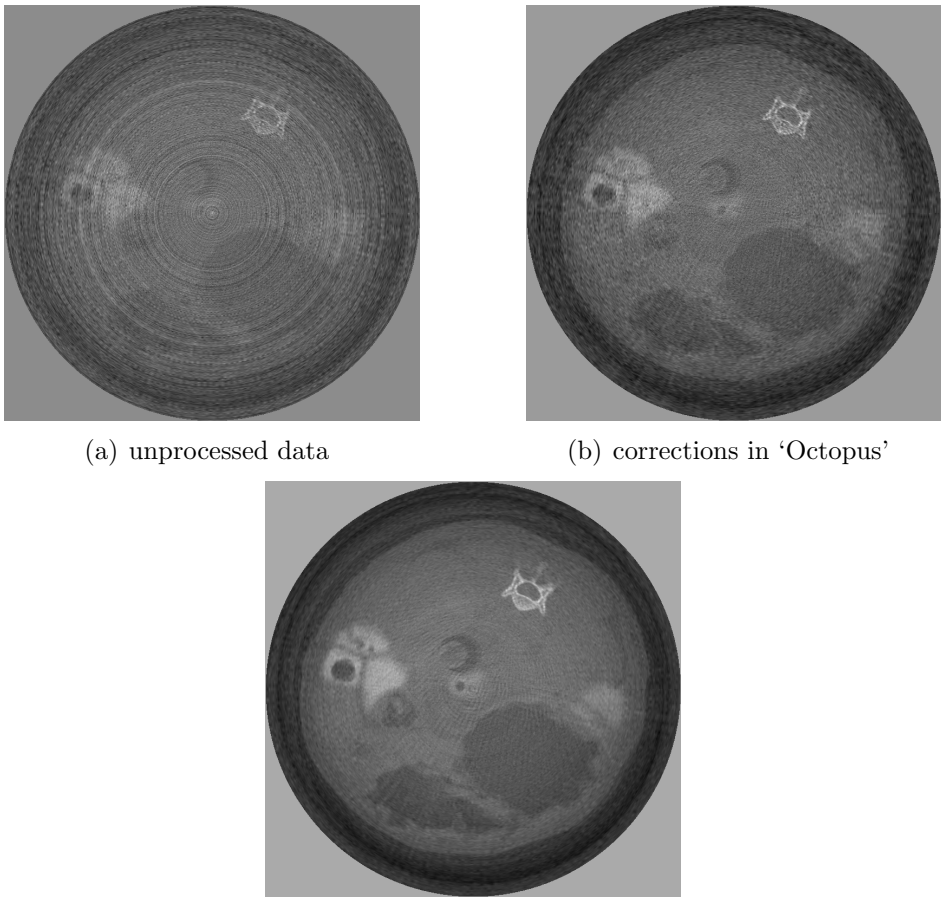

(a) unprocessed data

(b) corrections in 'Octopus'

(c) our corrections

Figure 3.11: Resulting CT slices for different methods of image processing.

Discussions with the developers of 'Octopus' from Ghent University were very fruitful and eventually might lead to a version of 'Octopus', especially optimised for the Medipix detector.

3.9 Summary

This chapter provided an overview of the image correction techniques and the CT back projection. All pre-reconstruction steps that are performed in the software tool 'Octopus' have been successfully implemented in Matlab, some have been optimised for our needs. Flatfield acquisitions with a Perspex slab in the field of view simulate for the alteration of the spectrum by the

object. A new technique offers the possibility to normalise the flux between different detector positions. The method of finding and interpolating noisy pixels has been improved. The quad configuration demanded new methods of interpolation which have been successfully performed. Furthermore, a ring-artefact filter has been implemented.

This work was presented at the 'Engineering and Physical Sciences in Medicine and the Australian Biomedical Engineering Conference' in November 2008 in Christchurch, New Zealand. Furthermore, it has contributed to a publication and presentation at the 'International Symposium on Peaceful Applications of Nuclear Technologies in the GCC Countries' which took place in Jeddah, Saudi Arabia in November 2008 [Butler et al., 2008].

Chapter IV

Evaluating spectral datasets

The aim of this chapter is to evaluate the relevant information contained in the spectral dataset. Two approaches are discussed in detail. The first technique works on the projections. To reconstruct the projected density of base materials, it uses knowledge of the energy-dependencies of the absorption coefficients and a maximum-likelihood estimation. The second approach applies the principal component analysis (PCA) to display the relevant information of the dataset in a few variables. These account for most of the variance contained in the dataset. We apply PCA to radiographs and on CT reconstructed slices.

4.1 The method of Material Reconstruction

The method of Material Reconstruction (MR) that Markus Firsching and the Medipix team in Erlangen have developed [Firsching, 2005] is described in this section. Suppliers of medical imaging systems have developed similar methods [Roessl and Proksa, 2007]. Data has been acquired together with Markus during his visit to our group. Then he sent us his processed images for further evaluation. The image correction techniques and the cone-beam CT reconstruction described in section 3 have been applied to the MR dataset.

The MR method uses a maximum likelihood estimation to reconstruct the partial contribution of different base materials to the projection images. Known input parameters are the base materials and their density ρ, their mass attenuation coefficient $\mu(E)$ and the incident spectrum $I_0(E)$. The projection images display the recorded intensity which for each pixel is given by the incident spectrum $I_0(E)$ multiplied by the transmittance T as expressed

by the following formula.

$$I(E) = I_0(E) \cdot T(E) = I_0(E) \cdot \exp(-\sum_{j=1}^{n} \mu'_j(E) p_j) \tag{4.1}$$

Here, $\mu'_j(E) = \mu_j(E)/\rho$ denotes the normalised mass attenuation coefficient μ which is dependent on the energy E. The projected density is given by $p_j = (\rho d)_j$ where ρ is the known density of the material j with n different materials. The path length that the photons traversed through this particular material is given by d. The algorithm aims to extract the projected density p_j.

In order to calculate the projected density p_j, the logarithmized transmittance $y_i = -\ln(I(E_i)/I_0(E_i)) = \sum_j \mu'_j(E_i) p_j$ is introduced. This equation can be written in matrix notation as a linear equation $\mathbf{y} = \mathbf{Mp}$ with the mass attenuation matrix M given by

$$M = \begin{pmatrix} \mu'_{E_1,m_1} & \mu'_{E_1,m_2} & \cdots & \\ \mu'_{E_2,m_1} & \mu'_{E_2,m_2} & & \\ \mu'_{E_3,m_1} & \mu'_{E_3,m_2} & & \\ \vdots & & \ddots & \\ & & & \mu'_{E_k,m_n} \end{pmatrix} \tag{4.2}$$

The subscription E_i denotes the $i = 1 \ldots k$ energy bins, the subscript m_j the $j = 1 \ldots n$ different materials.

The rank of this system of linear equations is k, the number of energy bins used which is chosen to be larger than the number of distinguishable base materials n. The method of least square fit can be used to find an approximate solution for the set of parameters p_j to the overdetermined system of linear equations.

In our case, the system of equations is given by $y = Mp$ and a least square

fit of the parameters that solve this equation is given by

$$p = (M^T M)^{-1} M^T y = M^+ y \tag{4.3}$$

where M^+ is the pseudoinverse of M.[Firsching et al., 2004]

While M can be seen as a transformation between the parameter space and the measured $-\log(T)$ component, M^+ performs the reverse transformation.

Our calculations so far were made under the assumption that the incident spectrum doesn't change and is monoenergetic. To derive the exact term for M, we need to consider the effects of beam hardening and the fact that the incident spectrum is polyenergetic which alters equation 4.1. This leads to a dependency of M from p_j which can be solved by an iterative algorithm.

As a first step, the spectrum $S(E)$ of the incident x-rays is considered. When performing measurements at a synchrotron with a high photon flux, one can afford to filter the energy of the incident beam resulting in an almost mono-energetic spectrum. For general applications, especially in medicine, this is not practicable and usually x-ray tubes are used to create photons in a broad spectrum such as in figure 2.9. With such a spectrum $S(E)$, equation 4.1 for only one material can be written as

$$I(E)/I_0(E) = \frac{\int_{E_1}^{E_2} \exp(-\mu'(E)p) \cdot S(E)dE}{\int_{E_1}^{E_2} S(E)dE}$$

When transmitting through material, the incident spectrum changes due to absorption which affects the low-energy photons much more than high-energy photons. This effect is called beam-hardening. Therefore the effective spectrum depends on the material prior traversed and can be given at the position l by

$$S_{eff}(E, l) = \exp(-\sum_{j=1}^{l-1} \mu'_j p_j)$$

It is here assumed, that the materials are arranged in arbitrary order where l denotes the position of the material currently traversed.

Given those two corrections, the formula from which we aim to deduce p_l is given by

$$T_{eff,l} = \frac{\int_{E_1}^{E_2} \exp(-\mu'_l(E)p_l) \cdot S_{eff}(E,l)dE}{\int_{E_1}^{E_2} S_{eff}(E,l)dE} := \exp(-\mu'_{eff,l}p_l)$$

This equation can be re-arranged to give

$$\mu'_{eff,l} = -\frac{1}{p_l}\ln(T_{eff,l})$$

The only problem is now that $\mu'_{eff,l}$ which we wish to use to find p_l is dependent on p_l itself.

The solution to this is an iterative approach where initial start values for p are chosen from which $\mu'_{eff,l}$ is calculated. These are used to calculate the complete matrix M of absorption coefficients as stated in 4.1. The matrix equation $y = Mp$ can be solved by a least square fit giving a new guess for p via $p = M^+y$. The measured data y is used as an input parameter. Now this new guess for p is used to calculate $\mu'_{eff,l}$ again. This process continues until finally a good set of parameters p is found.

4.1.1 CT reconstructing MR data

The material reconstruction algorithm has successfully derived the projected density $p_j = \int \rho_j(x,y)ds$ in each pixel for each base material j. It can be seen as a projection of the partial density $\rho_j(x,y)$ along the path s. Therefore, it is possible to use the reconstructed matrix of p_j to obtain the function $\rho(x,y)$ via the inverse radon transform. It is performed as part of the filtered-back projection (FBP) algorithm. The FBP expects a function $T = \exp(\int \mu(s)ds)$ as an input parameter and applies a negative logarithm as a first step to obtain a measure of the function $\int \mu(s)ds$. To skip this step, the negative exponential is applied to the data as explained in 3.1.2 before treating it with the filtered back-projection.

4.1.2 Limits of the method

Extensive calibration measurements of the spectral response of the detector to a monochromatic x-ray beam are necessary in order to deconvolve the incident spectrum of the x-ray tube $S(E)$. Furthermore, in order to invert M,

it must be of full rank - i.e. it must contain linearly independent components. Therefore, the maximum number of distinguishable materials is limited to the number of dominating physical effects which determine the number of linearly independent components of the mass attenuation matrix M. With two high-Z contrast agents, the relevant effects in the range between 10 and 150 keV are the photoelectric effect, Compton effect and the two k-edges allowing to identify four materials.

4.2 Evaluating spectral information with PCA

The previous section describes an established method that works on the projection dataset. We wanted to develop an alternative method of evaluating spectral data.

The method of principal component analysis seemed suitable allowing to identify linearly independent patterns of variance within a dataset. It can be used to reduce the dimensionality of the data by describing the important features of the dataset in only a few images. These show an enhanced contrast thus allowing an easier interpretation.

In order to evaluate the potential of PCA on spectral images from the Medipix detector, several datasets were used. The first set consists of 65 acquisitions of a Swiss watch (Swatch) and was acquired at CERN in 2006. The second dataset were seven radiographs of a foetal hand acquired in Christchurch in 2007. Furthermore, we applied the method of PCA to CT reconstructed slices from the 'mouse-2' dataset. Methods of displaying the derived information are discussed including cluster analysis and RGB colour mapping.

4.2.1 The method of PCA

Introduction to PCA

The principal component analysis (PCA) was derived in the beginning of the 20th century even though the basic idea behind the PCA existed since the 19th century known as 'Singular Value Decomposition'. But it wasn't until the 1990s, that advances in personal computers made it possible to

apply the method of PCA to the field of imaging and pattern recognition [Butler, 2007]. Since then it has been used in many fields ranging from voice recognition to medical imaging, e.g. [Bones et al., 2006]. In our case the analysis is performed on acquisitions taken of the same object in different spectral bands. This is different to applications in pattern recognition where images of different objects are compared that vary in spatial configuration.

PCA is widely used in analysis of multi-spectral reflectance images obtained in the visible and near infrared spectral band. Applications include quality assessment in food inspection [Mehl et al., 2004], chemical science [Winson et al., 1997] and space science [Stephan et al., 2008] where it has been successfully used to reduce instrument-dependent noise. A good description of the application of PCA to multi-energy data acquired from different x-ray spectra is given in [Kalukin et al., 2000].

Mathematical derivation of the PCA method

In the following, the mathematical formulation of principal component analysis will be described in order to introduce the notation we use. More detailed derivations and their proofs can be found in literature, e.g. [Jollife, 2002].

For every chosen energy, $i = 1 \dots k$, we measure an image of p pixels. Each image at a particular energy is represented by the row vector $\mathbf{x}_i$ in which each element x_{ij} contains the intensity value of one pixel where $j = 1 \dots p$. For spectroscopic x-ray images there are typically far fewer energy bins than pixels. That is, $k \ll p$.

In order to simplify further calculations, each pixel's intensity value is centred by subtracting $\langle \mathbf{x}_j \rangle$, the average intensity over all energies which is given by equation 4.4.

$$a_{ij} = x_{ij} - \langle \mathbf{x}_j \rangle = x_{ij} - \sum_{i=1}^{k} x_{ij}/k. \tag{4.4}$$

For further evaluation, it is beneficial to combine all data into one matrix A where each element is given by a_{ij}. In this representation, the j^{th} column is the centred energy spectrum for the j^{th} pixel, while the i^{th} row of A is the centred image $\mathbf{a}_i$ at the i^{th} energy.

Having established a notation for our dataset, we can now proceed by performing the relevant steps for principal component analysis. The matrix of co-variances for a sample distribution of k centred images is given by equation 4.5. It gives a measure for the linear dependencies amongst the vectors $\mathbf{a}_i$. Its rank, at most k, gives the number of independent components within the data [Jollife, 2002].

$$C = \frac{1}{k-1} A \cdot A^T \tag{4.5}$$

It can be shown that the eigenvectors corresponding to the highest eigenvalues of C account for directions of maximal co-variance in the data. When arranged in decreasing order of eigenvalues λ_i, the k eigenvectors $\mathbf{u}_i$ can be used as base vectors to transform the data matrix A onto a new coordinate system given by $\mathbf{z}_1, \ldots \mathbf{z}_k$ as expressed in equation 4.6. This vector space can be referred to as eigenspace.

$$\mathbf{z}_i = \mathbf{u}_i^T A = \sum_{l=1}^{k} \mathbf{u}_{il}\, \mathbf{x}_l \tag{4.6}$$

In engineering literature, the eigenvectors $\mathbf{u}_i$ are typically called 'principal components', although Jollife notes that some authors call $\mathbf{z}_i$ the principal component and refer to $\mathbf{u}_i$ as the vector of loading [Jollife, 2002]. We adopt the notation from engineering literature calling $\mathbf{u}_i$ 'principal components'. To avoid confusion, we name the transformed vectors $\mathbf{z}_i$ 'PC-images'. It is worth noting that $\mathbf{z}_i$ have a mean of zero and a variance of λ_i.

4.2.2 PCA applied to projection images

Watch dataset

The first dataset that we used for testing this technique was a series of radiographs of a watch. They were obtained with a tungsten target x-ray tube with 2.5 mm Al filtration, operated at 50 kV. The detector was set to count photons in an energy bin of the fixed width of 3.1 keV. The lower energy threshold was shifted between 13 and 46.8 keV and 56 images have been acquired with a step size of approximately 0.6 keV and 150 mAs illumination.

Figure 4.1 shows two examples from the dataset. For the left image, the energy bin was set between 13 keV and 16.1 keV, to the right image only photons with an energy between 44.9 and 48 keV contributed. In the image from the high energy bin, the gear-wheels behind the cover are better visible. This is due to the fact that many of the high-energy photons are transmitted through dense areas, while low-energy photons are mostly absorbed, resulting in a hardening of the beam. In this case, detecting only high-energy photons leads to an improved contrast and better detail recognition.

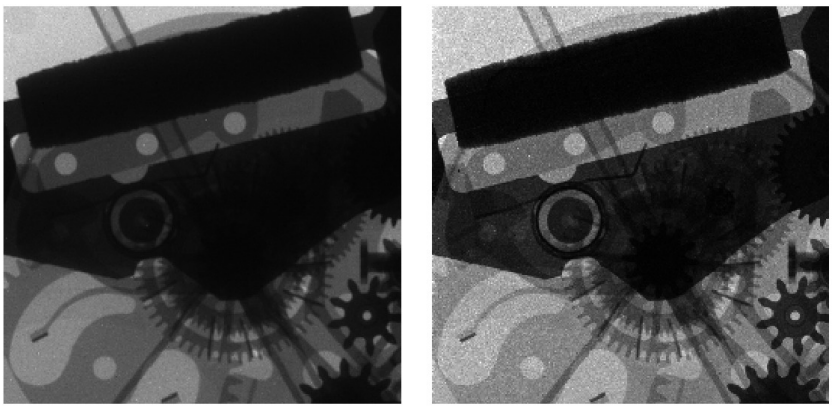

Figure 4.1: Images from the spectral dataset of a watch; low energy bin (left) and high energy bin (right).

We now test if the method of PCA, by aiming at maximising the variance in the data and at the same time reducing redundancies, can find such significant features in a large dataset. Following the notation introduced in section 4.2.1, the centred data matrix A has a size of $k = 56$ by $p = 256 \times 256 = 2^{16}$ elements, where p gives the number of pixels in each of the k images.

Figure 4.2 shows a plot of the first three derived principal components or "eigenspectra". Since the i^{th} element of each principal component corresponds to the i^{th} energy bin it is possible to label the x-axis of this plot with energy. Any pixel's spectrum can be reconstructed as a linear combination of the eigenspectra plus the average spectrum. Three non-noisy eigenspectra could be identified which implies that there are at least three patterns of independent variance within the spectral data. Spectra of higher order show

increasing fluctuations.

According to equation 4.6, the elements of the i^{th} eigenvector give a weighting factor for each centred image which determines its contribution to the i^{th} PC-image $\mathbf{z}_i$.

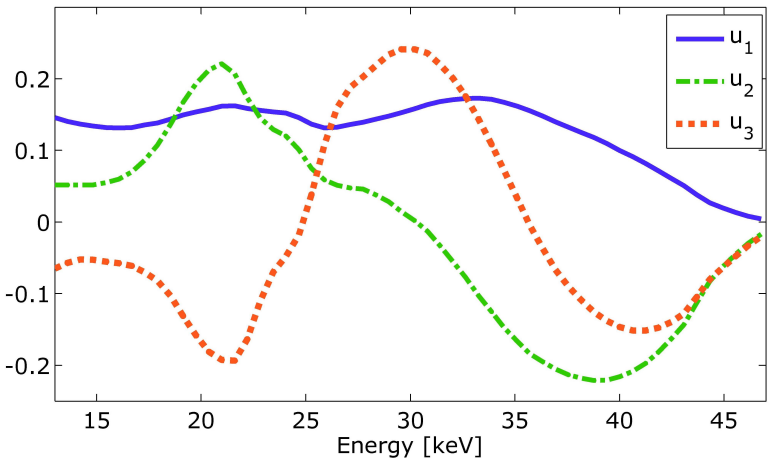

Figure 4.2: The first three eigenvectors which define the contribution of each centered image to the first three PC-images.

The 2^{16} elements of the vector $\mathbf{z}_i$ can be reshaped to a 256×256 pixel matrix leading to a representation of the image in the i^{th} eigenspace, as can be seen in figure 4.3. While these images are closely related to eigenimages commonly found in pattern recognition they are not identical to them. In particular, we have centred our data in the energy domain rather than the spatial domain before analysing the variance.

From the k PC-images, only the first three contain useful information. With increasing order, the noise in the PC-images dominates and images show no useable information. So the high redundancies of the original 56 images have been removed leading to a representation of the relevant information in the first three eigenspace images.

The first PC-image shows a much better signal-to-noise ratio than any of the single acquisitions. Looking at the first eigenvector in figure 4.2 reveals that all original images have almost equally contributed to this component which leads to a reduction of the statistical noise.

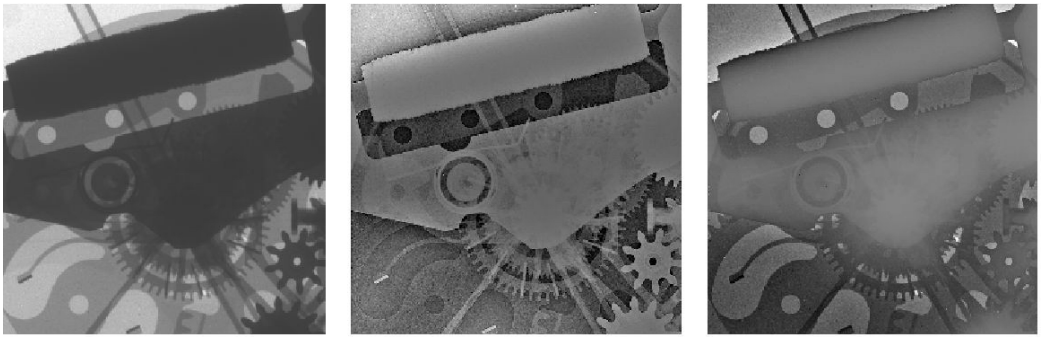

Figure 4.3: The first three PC-images hinting at differences in the dataset.

Each eigenvector is by definition linearly independent and therefore the PC-images highlight subtle changes in the dataset. Some regions change their intensity values significantly between two PC-images while the other regions remain at similar intensities. This can be seen for example in the darkest region of the first PC-image in comparison to the third PC-image in figure 4.3. It highlights the effect of beam-hardening which is the main difference that occurs in the whole dataset, as explained above.

Cluster analysis of watch data

In order to further investigate differences in the transformed variables, we plotted the location of the first three principal components in eigenspace as a scattergram, as can be seen in figure 4.4. Each point represents one pixel, the location on the x-axis is given by the intensity value of the first PC-image (left image in figure 4.3), the intensity value of the second and third PC-images give the location on the y-axis and the colour respectively.

Most of the variance can be found along the **x** axis, but the second and third PC-images also contribute to a separation of individual clusters. e.g. separating region '2' from region '3' in figure 4.4. This demonstrates again that at least three patterns of variance are contained within the spectral data.

The information can be displayed in a single image, where each of the identified clusters is given a colour as in figure 4.5. Each cluster represents a group of pixels that have similar spectra. It is a non-trivial result that

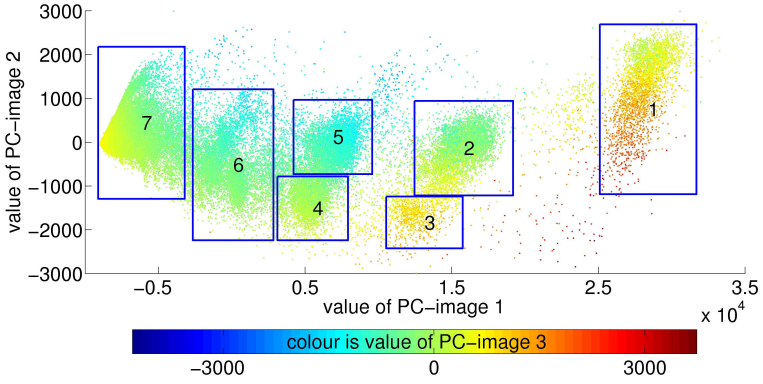

Figure 4.4: Scattergram where each data point represents one pixels intensity value in PC-image z_1, z_2 and z_3.

clustering in eigenspace leads to a grouping of neighbouring pixels. As can be seen from the example of region '2' (green) and '3' (red), areas that could not been distinguished from any single images of the unprocessed dataset, can now be separated.

PCA of foetal hand

A spectroscopic dataset consisting of seven acquisitions with variation of only the lower energy threshold from 4-27 keV of the hand of a 20 week old miscarried foetus were acquired with an x-ray tube with a peak voltage of 35 kV. One can see the bones that are not yet fully developed.

The principal component analysis has been applied in the same way as described above for the watch dataset. This time, the first three PC-images $\mathbf{z}_1$, $\mathbf{z}_2$ and $\mathbf{z}_3$ have been combined into one red-green-blue (RGB) image, figure 4.6. In this image, $\mathbf{z}_1$, $\mathbf{z}_2$ and $\mathbf{z}_3$ are assigned a colour channel (red, green or blue) each.

The representation of the dataset as one RGB image leads to an advanced contrast that combines all relevant information of the dataset. It can clearly be seen that the bone (blue) has a different energy response than the soft tissue (green). The red area at the top right of the image is thought to relate

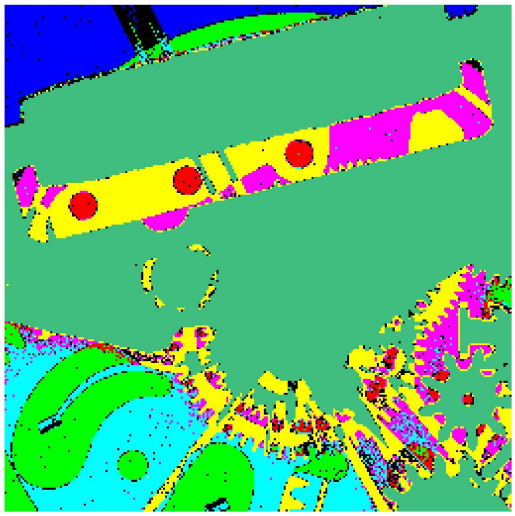

Figure 4.5: Colour map of identified clusters which partly show groups of similar materials.

to variations in the detector response.

4.2.3 Extending PCA to CT data

In the above section we've explained how the principal component analysis can be applied to radiographs. It enhanced the contrasts and identified important features from the dataset, but could not be used to uniquely identify materials, as the intensity value for different material changes with varying thickness. Furthermore, materials are typically overlapping.

PCA analysis of 'mouse-2' data

Therefore, the next step was to apply PCA to a set of CT reconstructed slices with the aim of identifying separate materials. We chose the four energy bins from the 'mouse-2' dataset with each slice of the size 768×768 pixels. The original dataset can be seen in figure 5.2. In the first and second energy bin image, the intensity of the contrast agent and the spinal bone is not distinguishable, but the images show a good contrast and little noise. The

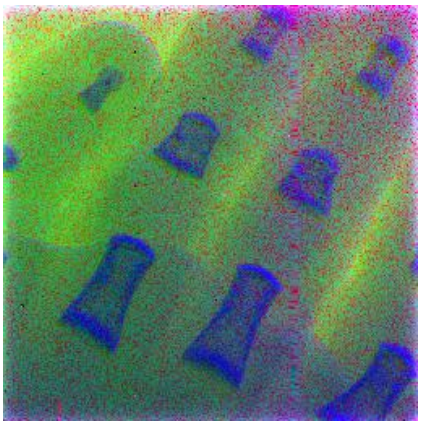

Figure 4.6: Foetal hand with the RGB colour map given by the first three PC-images $\mathbf{z}_1$, $\mathbf{z}_2$ and $\mathbf{z}_3$.

third energy bin on the other hand allows distinguishing both, but shows a lot more noise. The fourth energy bin contains almost solely noise. To evaluate the data, typically only the first energy bin would be used due to its good image quality. However, the additional information from the high energy bins can be included in the analysis using the method of PCA. The PCA calculations performed are the same as for the radiographs which were explained above in section 4.2.2. The original dataset is intensity centred and the covariance matrix is calculated. Its eigenvectors are then determined which can be seen in figure 4.7. They define the contribution of each energy bin slice to the PC-images which are shown in figure 4.8.

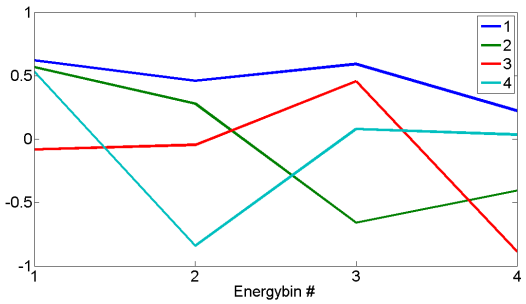

Figure 4.7: Eigenspectrum for 'mouse-2' dataset showing the contribution of each energy bin to the four PC-images

Almost all energy bins have contributed equally to the first PC-image. The result is an image similar to energy bin 1 but with slightly worse image quality due to additionally introduced noise and ring artefacts from the higher energy bins. Therefore, in contrast to the series of radiographs from the swatch dataset, the contrast could not be enhanced due to the small number of contributing images and their bad image quality. The second PC-image shows the spinal bone (top right) isolated without the contrast agent. This is the key information which we aimed to extract. The other two components show mainly noise patterns.

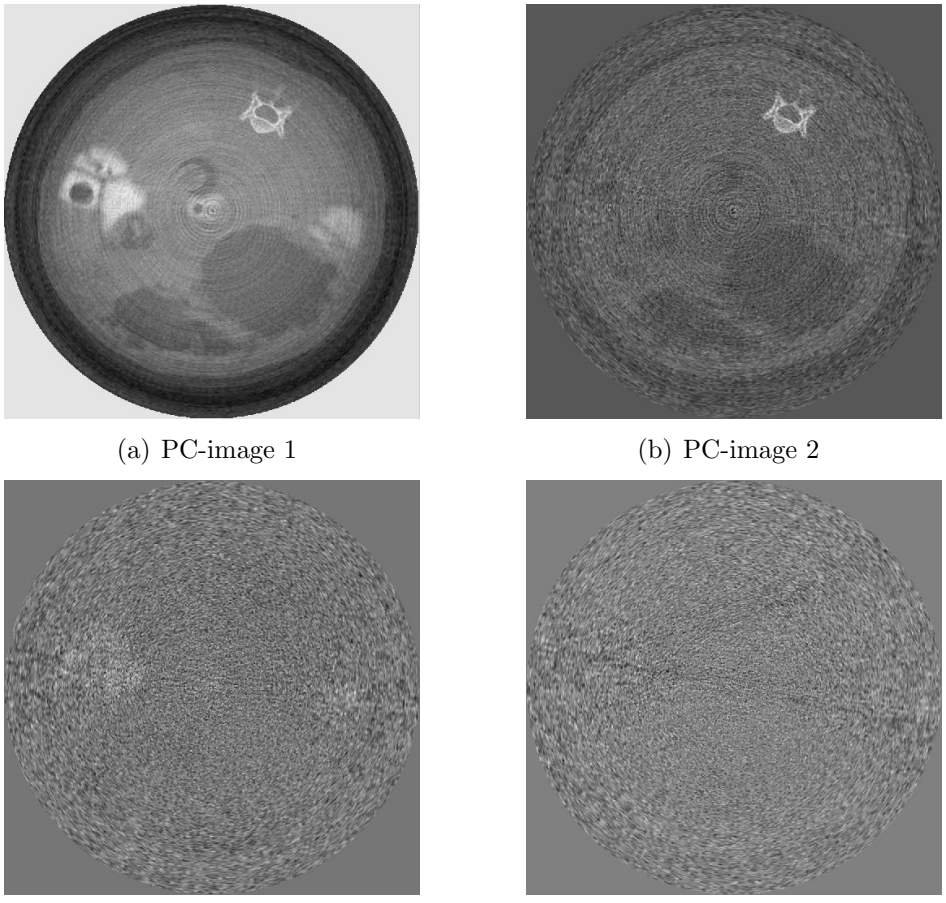

(a) PC-image 1

(b) PC-image 2

(c) PC-image 3

(d) PC-image 4

Figure 4.8: PCA applied to slices from the 'mouse-2' dataset.

Displaying PC-image 1 and 2 as two colours in one image can be used to

highlight this information. In this image shown in figure 4.9, the spinal bone and contrast agent are clearly distinguishable.

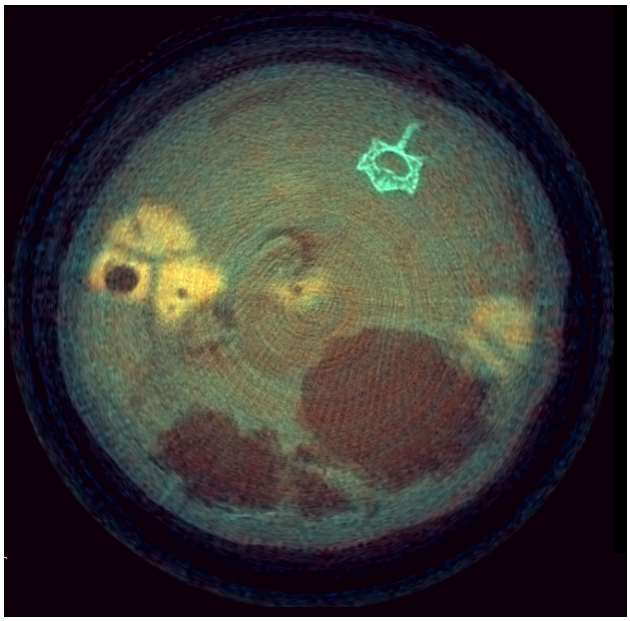

Figure 4.9: Combined image of the first two PC-images from the 'mouse-2' dataset.

Cluster analysis of PCA data

A cluster analysis using the first three PC-images can be performed, the resulting scattergram can be seen in figure 4.10. Four separate regions have been identified which correspond to separate materials. Each region is given one colour and all regions are displayed in one image as shown in figure 4.11. The blue cluster shows the locations of the iodine contrast agent, the green region is the spinal bone. The perspex tube is defined by the red cluster region and the pink coloured cluster shows the rest. Thus, it was successful to separate four materials, in particular the contrast agent iodine and the spinal bone. As not all data points in the scattergram have been selected, not all structures are shown in the combined image.

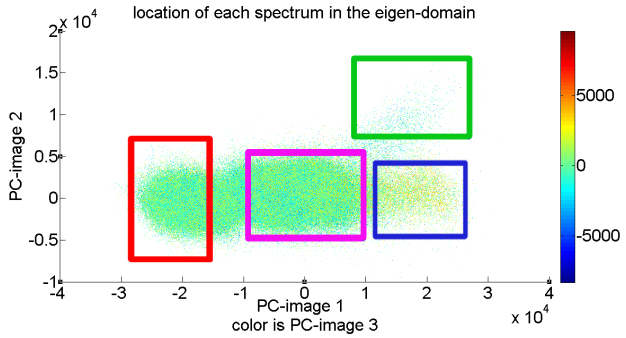

Figure 4.10: Cluster analysis of PC-images from 'mouse-2' dataset with four identified regions.

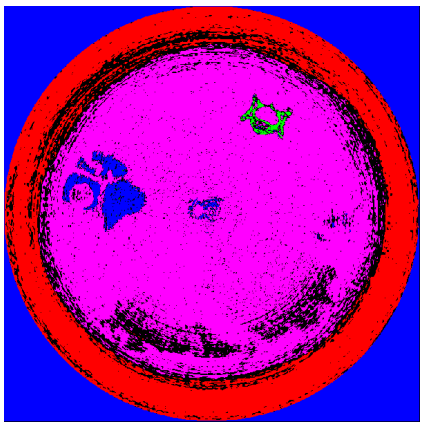

Figure 4.11: Identified materials from the cluster analysis.

PCA on volume datasets

The next step was to extend the PCA method to be useable for a whole volume dataset. Calculating the covariance matrix and deriving its eigenvectors for each slice individually would be computationally expensive. Therefore, we used the eigenvectors from a single slice to transform the whole dataset onto a new basis. Consequently, four PC-images are derived for each slice. Such a method is similar to the application of PCA to face recognition where principal components are derived using a small training set of face images. New faces, not from the training set, are then described as a linear combination of the principal components. This method has been successfully applied to all reconstructed slices from the 'mouse-2' dataset.

Results

The PCA method has successfully reduced the number of relevant images from 4 to 2. The key information which is the difference between contrast agent and bone has been successfully extracted in the second PC-image. Unfortunately, noise patterns such as ring artefacts are also regarded as structures in the PCA method and have been enhanced. The low number of input images and the bad image quality of half of them is certainly one reason for this. However, combining the two PC-images in one colour image showed a good quality and included the difference between contrast agent and bone. The method of cluster analysis showed that different materials are located in different places in the eigen-domain. This allowed identifying unique materials and displaying them in one combined false-colour image. The method has been extended to be suitable for a volume dataset.

4.2.4 Ideas for further improvements

In the future, the cluster analysis could be extended further. Reference materials can be scanned and their unique location in eigen-space can be used to analyse a new sample and give an estimation of the materials contained therein. Furthermore, new methods of displaying the PC-images additionally to the normal dataset can be investigated. It could be possible to further improve segmentation by combining the PCA method with a method that uses spatial information.

The next version of the Medipix detector will allow simultaneous measurement in up to eight energy bins [Ballabriga et al., 2006]. This will give identical Poissonian noise across all energy bins, which should make it easier to evaluate spectral data.

4.3 Summary

In this chapter, two methods of evaluating spectral data have been presented. The method of material reconstruction has been developed by Markus Firsching. It uses a maximum-likelihood estimation in an iterative approach and could be successfully used to reconstruct images of base materials. With

two contrast agents with high k-edges, up to four materials can be distinguished. The method of principal component analysis was newly introduced to the field of Medipix imaging. First trial studies on data from a swatch showed how the first few principal components display most of the information in the dataset. A cluster analysis could be performed where regions in the eigen-domain lead to neighbouring pixels. With images from a foetal hand, the method of RGB remapping has been introduced. It showed how the information from several energy bin images can be combined via the PCA method in one single colour image. Finally, applying the PCA method to CT slices of the 'mouse-2' dataset reduced the number of non-noisy images from four to two, thus removing redundancies. At the same time, the spinal bone and contrast agent were separated in these PC-images. Here again, displaying the PC-images in one colour image combines all the information from the dataset. The method of cluster analysis could also be performed resulting in four separate regions of different materials. The work on the PCA method has been summarised in a presentation and publication at the '23rd International Conference on Image and Vision Computing New Zealand' held in November 2008 in Christchurch, New Zealand. Furthermore, it has contributed to a presentation at the 'Society for Imaging Informatics in Medicine' annual meeting which takes place in Charlotte, USA in June 2009.

Chapter V

Results from biomedical studies

This chapter gives an overview of the results obtained from biomedical studies. The biological structures visible in 'mouse-2' are discussed in the slice from the first energy bin. Then the whole dataset is analysed including the material reconstructed data and the PC-images. Finally, examples of further contrast agent studies are given.

In slices from the first energy bin of the 'mouse-2' dataset, several anatomical regions can be identified as indicated in figure 5.1. Amongst those are the spinal bone, the lumbar triangle, the bowel and the stomach. In some slices, the stomach wall is visible and some show bubbles of gas or faecal material within the bowel. There are some movement artefacts in the bowel which don't appear in the spinal bone. This could be explained by decomposition of bowel contents or movement of bowel gas. In few slices, there is a high attenuation object in or on the abdominal wall. The source of this high attenuation is unknown but could result from a drop of iodine on the mouse's skin or a small piece of metal in the mouse's fur.

The reconstructed slices from all energy bins of the 'mouse-2' dataset can be seen in figure 5.2. With increasing low energy threshold THL, the noise in the images increases as less and less photons contribute. In the first and second energy bin image, the intensity of the contrast agent and the spinal bone is not distinguishable. The third energy bin image allows one to distinguish both, but shows a lot more noise and new ring artefacts. The fourth energy bin slice contains almost solely noise. In the material reconstructed images of the partial density of water and iodine the latter is clearly isolated while the 'water' image is similar to energy bin 1 image without the contrast agent. The material reconstruction thus successfully separated the contrast agent from the rest of the image.

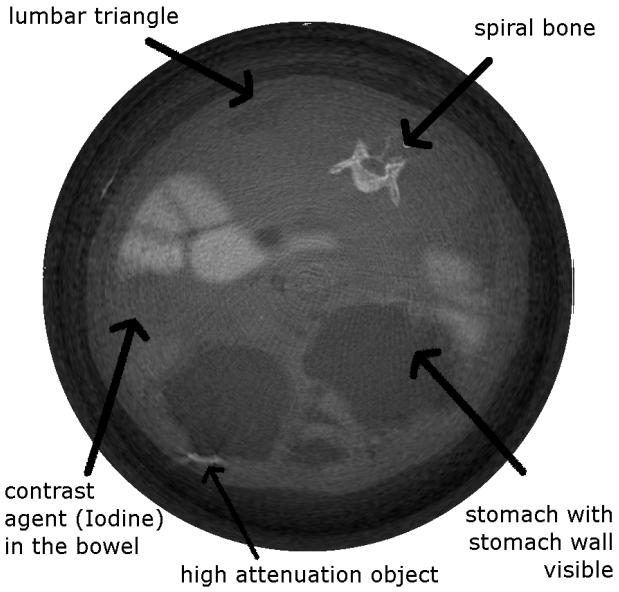

Figure 5.1: Commented slice from 'mouse-2' dataset, energy bin 1 (> 12 keV).

Images from the PCA method applied to the 'mouse-2' dataset are shown in figure 4.8. Here, in the second PC-image, the spinal bone has been isolated from the rest of the image. A combination of the first two PC-images as two colours in one image can be seen in figure 4.9. In this image, both spinal bone and contrast agent are highlighted in a different colour.

So in comparison, the PCA method optimised the variance in the dataset, while the processed slices from the MR algorithm show the partial density of the base materials. The PCA method shows a better image quality which is understandable, as the MR data was binned for processing. The MR algorithm is capable of isolating the contrast agent, while the PCA method has isolated the spinal bone. Creating a combined colour image for both methods results in a separation of bone and contrast agent in one image.

As described in section 3.2.1, several contrast agent studies have been performed by our team. One result of such a study with 'mouse-10' can be seen in figure 5.3. It shows the pulmonary tree in the lungs, where the contrast agent barium has been used to highlight the vascular system. Ribs

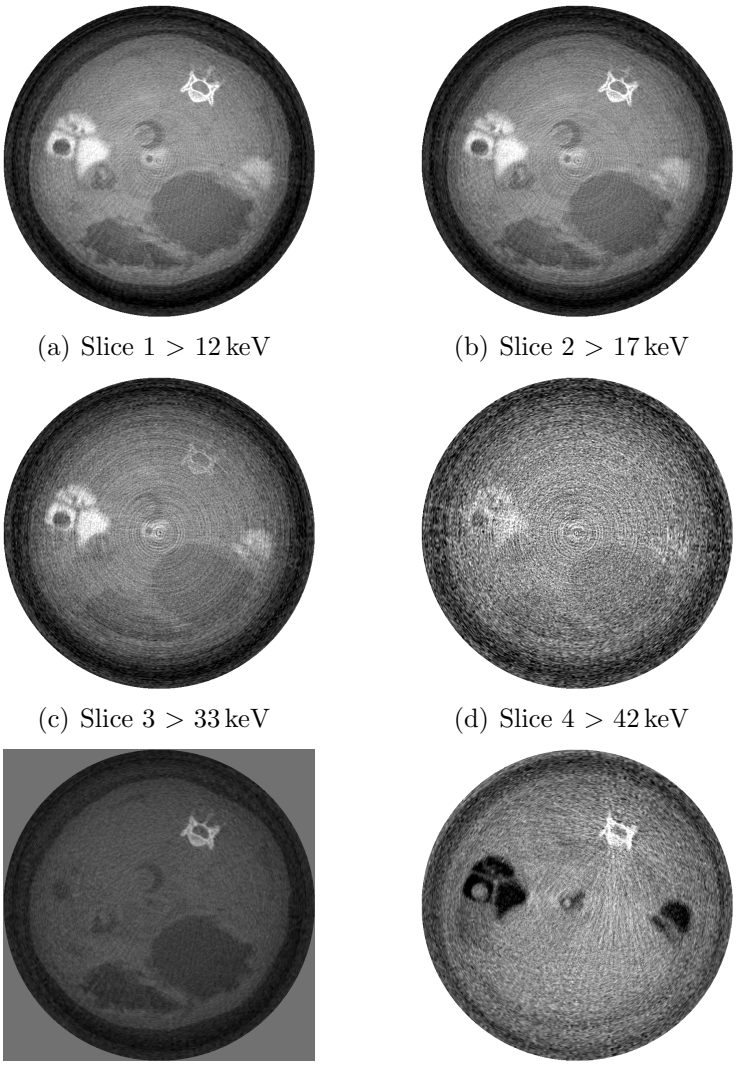

(a) Slice 1 > 12 keV (b) Slice 2 > 17 keV

(c) Slice 3 > 33 keV (d) Slice 4 > 42 keV

(e) MR slice 'Water' (f) MR slice 'Iodine'

Figure 5.2: CT slices from the 'mouse-2' dataset in four different energy bins and two MR slices.

and the spinal bone can be seen as well. Further studies have been performed with multiple energies and on other mice with multiple contrast agents.

In conclusion, we could show that contrast agent imaging with MARS-CT is feasible and reveals several anatomical details. This prepares the way for future studies. The work in this chapter has contributed to a presentation on the 'European Society of Radiology' congress which took place in Vienna,

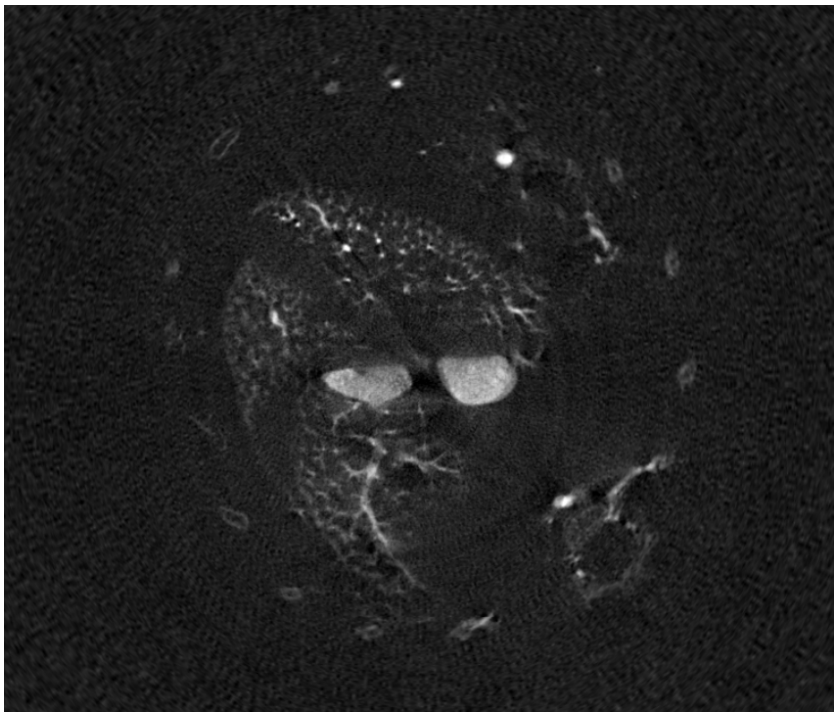

Figure 5.3: Reconstructed slice from lung region of 'mouse-10' showing the vascular system highlighted via the contrast agent.

Austria in March 2009.

Chapter VI

Conclusion

Dual-energy CT has brought spectral x-ray imaging into clinical reality and proven its benefits and potential in numerous applications. Our goal was to introduce Medipix, a spectroscopic photon-processing detector to biomedical applications. Therefore, the 'Medipix All Resolution System' scanner MARS-1 was constructed. Initial experiments with the MARS-1 setup provided first results from a contrast agent study. However, the scanner setup was unstable and the images needed further processing. While the scanner was upgraded to the MARS-2 setup, image correction techniques have been developed. These are important, as they could correct for some of the weaknesses of the setup such as fluctuations between different detector stops and uneven pixel responses. For the latter, a ring-artefact reduction technique has been implemented. Noise was especially prevalent in base material projections from the material reconstructed dataset. The image correction techniques for the initial and improved setup are described in chapter 3. The scanner upgrade resulted in a stable software and no fluctuations between different acquisitions. The detector has been successfully replaced by a quad array of chips, missing rows and columns have been interpolated leading to a continuous transition. It could be estimated that the focal spot of the x-ray tube doesn't limit its performance in the current setup. The measured profile of the x-ray tube however results in some gradient over the width of the detector, especially in the quad version. In the fourth chapter, two different approaches for evaluating spectral data are presented. The first method is the material reconstruction which has been applied to the raw data of the initial experiments with MARS-1 by Markus Firsching. It produced projections of 'water' and 'iodine' base materials which have been treated by the image correction methods and resulted in slices of the partial density of those materials. The iodine is clearly separated from the spinal bone and

other body structures. As a second method, the principal component analysis (PCA) was introduced. It allowed us to transform the original images onto a base of maximal variance. First tests of this method applied to radiographic datasets were successful reducing redundancies in the data and highlighting differences that occur between the images. A cluster analysis leads to grouping of neighbouring pixels. Appling the PCA method to CT slices resulted in PC-images that could be combined into one coloured image where the spinal bone and the contrast agent are separated. The next steps of our group is to investigate further applications of MARS-CT. Work has begun on studies that focus on multi-contrast agent imaging and measuring the fat content of the liver. It is planned to construct a scanner optimised for mammography and eventually a full-body CT scanner with Medipix detectors. At the present time, MARS-3 is being assembled.

Chapter VII

Conferences

1. J.S. Butzer, A.P. Butler, N.J. Cook, P.H. Butler, F. Ross, N. Schleich, J. Selkirk, R. Watts, J. Meyer, N. Scott, P.J. Bones, D. van Leeuwen, S. Hemmingsen, T.R. Melzer and N. Anderson. MARS: A 3D spectroscopic x-ray imaging device based on Medipix. *IEEE Medical Imaging Conference, October 2008, Dresden, Germany.*

2. J.S. Butzer, A.P. Butler, P.H. Butler, N.J. Cook, N. Schleich, M. Firsching, N. Scott, N. Anderson, P.J. Bones, F. Ross, R. Watts, J. Meyer, D. van Leeuwen and J. Selkirk. Spectroscopic contrast-agent imaging with the Medipix CT-Scanner 'MARS'. *Engineering and Physical Sciences in Medicine and the Australian Biomedical Engineering Conference 2008, November 2008, Christchurch, New Zealand.*

3. J.S. Butzer, A.P. Butler, P.H. Butler, P.J. Bones, N. Cook and L. Tlustos. Medipix Imaging - evaluation of datasets with PCA. 23*rd International Conference Image and Vision Computing New Zealand, November 2008, Christchurch, New Zealand.*

4. P.H. Butler, A.J. Bell, A.P. Butler, N.J. Cook, L. Reinisch, J.S. Butzer and N. Anderson. MARS Biomedical 3D spectroscopic x-ray imaging. *International Symposium on Peaceful Applications of Nuclear Technologies in the GCC Countries, November 2008, Jeddah, Saudi Arabia*

5. N. Anderson, A.P. Butler, N. Scott, N.J. Cook, J.S. Butzer, N. Schleich, P.H. Butler. Colour CT X-ray spectroscopic images of mice using Medipix-2 detector. *European Society of Radiology Congress, March 2009, Vienna, Austria*

6. A.P. Butler, J.S. Butzer, P.J. Bones, N. Schleich, M. Firsching, N.J. Cook. Enhancement of spectral computed tomography data using modified principal components analysis. *Society for Imaging Informatics in Medicine (SIIM) annual meeting, June 2009, Charlotte, USA*

Chapter VIII

Acknowledgments

I would like to thank Dr. Anthony Butler for his supervision, support and motivation, Prof. Phil Butler for his time and many fruitful discussions and Prof. Phil Bones for many good ideas for corrections on my written work. Additionally, I would like to thank my german supervisor Prof. Tilo Baumbach, especially for his support in preparation of my thesis.

Furthermore, many thanks to Dr. Nick Cook for all the fun we had working together. Thanks to Dr. Nanette Schleich for the long hours spent at the scanner and to Dave van Leeuwen for his help and support for computer soft- and hardware. In addition, I would like to thank Stephen Hemmingsen and his team at the workshop at Canterbury University and Kathreen, Michael and Johann from the workshop at Christchurch Hospital for their spontanous and professional help.

Thanks to Juergen Meyer and Richard Watts for help with Matlab coding of the ring-artefact filter. Furthermore, thanks to Jonathan Selkirk for his contribution to the energy calibration of the quad detector and to Fred Ross for his work on the calibration phantom for the scanner. Also thanks to Nicola Scott and Nigel Anderson for preparing the biological specimen.

A big thanks goes to all the members of the MARS team at the University of Canterbury and at Christchurch Hospital and the Medical School - you're a great team and I enjoyed very much working with you!

Special thanks to all the members of the Medipix collaboration, it is great to see such a motivated and diverse group working together. In particular, I would like to thank Markus Firsching with whom I have performed the first measurements and who explained a lot to me.

Thank you Robert, Svenja and Stephie for your help with proofreading this thesis.

I would like to thank the German Academic Exchange Service (DAAD) for supporting me financially during parts of my stay in New Zealand.

Last but definitely not least, I would like to thank my family for their support and help and especially my girlfriend Simone for everything she has done for me.

References

[Asaga et al., 1987] Asaga, T., Chiyasu, S., Mastuda, S., Mastuura, H., Kato, H., Ishida, M., and Komaki, T. (1987). Breast imaging: Dual-energy projection radiography. *Radiology*, 164:869–870.

[Autiero et al., 2005] Autiero, M., Celentano, L., Cozzolino, R., Laccetti, P., Marotta, M., Mettivier, G., Montesi, M. C., Riccio, P., Roberti, G., and Russo, P. (2005). Experimental study on in vivo optical and radionuclide imaging in small animals. *IEEE transactions on nuclear science*, 52:205–209.

[Ballabriga et al., 2006] Ballabriga, R., Campbell, M., Heijne, E., Llopart, X., and Tlustos, L. (2006). The medipix3 prototype, a pixel readout chip working in single photon counting mode with improved spectrometric performance. *Nuclear Science Symposium Conference Record, 2006. IEEE*, 6:3557–3561.

[Birch et al., 1979] Birch, R., Marshall, M., and Ardran, G. M. (1979). 1979 catalogue of spectral data for diagnostic x-rays. *Hospital Physicists Association Scientific Report Series 30 (IPSM, PO Box 303 York)*.

[Bisogni et al., 2007] Bisogni, M., Guerra, A. D., Lanconelli, N., Lauria, A., Mettivier, G., Montesi, M., Panetta, D., Pani, R., Quattrocchi, M., Randaccio, P., Rosso, V., and Russo, P. (2007). Experimental study of beam hardening artifacts in photon counting breast computed tomography. *Nuclear Instruments and Methods in Physics Research Section A*, 581:94–98.

[Bisogni et al., 2002] Bisogni, M. G., Fabbri, S., Gambaccini, M., Marziani, M., Novelli, M., Quattrocchi, M., Rosso, V., Russo, P., Sarnelli, A., Stefanini, A., and Zucca, S. (2002). A digital system based on a bi-chromatic x ray source and a single photon counting device: a single exposure dual energy mammography approach. *Proceedings of SPIE*, 4682:620–632.

[Blanchot et al., 2006] Blanchot, G., Chmeissani, M., Dz, A., Dz, F., Ferndez, J., Garc, E., Garc, J., Kainberger, F., Lozano, M., Maiorino, M., Martez, R., Montagne, J. P., Moreno, I., Pellegrini, G., Puigdengoles, C., Sent, M., Teres, L., Tortajada, M., and Ull, M. (2006). Dear-mama: A photon counting x-ray imaging project for medical applications. *Nuclear Instruments and Methods in Physics Research A*, pages 136–139.

[Bollini et al., 2003] Bollini, D., Rodriguez, A. E. C., Dabrowski, W., Garcia, A. D., Gambaccini, M., Giubellino, P., Grybos, P., Idzik, M., Marzari-Chiesa, A., Montano, L. M., Prino, F., Ramello, L., Sitta, M., Swientek, K., Wheadon, R., and Wiacek, P. (2003). Energy resolution of a silicon detector with the rx64 asic designed for x-ray imaging. *Nuclear Instruments and Methods in Physics Research Section A*, 515:458–466.

[Bones et al., 2006] Bones, P. J., Butler, A. P. H., and Hurrell, M. (2006). Enhancement of chest radiographs using eigenimage processing. *In Image Reconstruction from Incomplete Data IV, Proceedings SPIE*, 6316:12pp.

[Butler, 2007] Butler, A. (2007). *Eigenimage processing of frontal chest radiographs.* PhD thesis, University of Canterbury, Christchurch, New Zealand.

[Butler et al., 2008] Butler, P. H., Bell, A. J., Butler, A. P., Cook, N. J., Reinisch, L., Butzer, J. S., and Anderson, N. (2008). Mars biomedical 3d spectroscopic x-ray imaging. *proceedings of the International Symposium on Peaceful Applications of Nuclear Technologies in the GCC Countries, Jeddah, Saudi Arabia.*

[Campbell et al., 1990] Campbell, M., Heijne, E. H. M., Jarron, P., Krummenacher, F., Enz, C. C., Declercq, M., Vittoz, E., , and Viertel, G. (1990). A 10 mhz micropower cmos front end for direct readout of pixel detectors. *Nuclear Instruments and Methods in Physics Research A*, 290:149–157.

[Campbell et al., 1998] Campbell, M., Heijne, E. H. M., Meddeler, G., E.Pernigotti, and W.Snoeys (1998). Readout for a 64 x 64 pixel matrix

with 15-bit single photon counting. *IEEE Transaction on Nuclear Science*, 3(45):751–753.

[Dierick et al., 2003] Dierick, M., Masschaele, B., and Van Hoorebeke, L. (2003). Octopus, a fast and user-friendly tomographic reconstruction package developed in labview (r). *Proceedings of the Third World Congress on Industrial Process Tomography, Banff, Canada*, pages 571–576.

[Doessel, 2000] Doessel, O. (2000). *Bildgebende Verfahren in der Medizin - Von der Technik zur medizinischen Anwendung*. Springer-Verlag.

[Ewald, 2007] Ewald, G. (2007). Vorbereitende messungen und simulationen fuer die untersuchung des medipix2 mit cdte als sensormaterial. Master's thesis, Physikalisches Institut der Friedrich-Alexander-Universitaet, Erlangen-Nuernberg.

[Fanti et al., 2003] Fanti, V., Marzeddu, R., and Randaccio, P. (2003). Mprs: Medipix parallel readout system for angiography digital imaging. *IEEE Transactions on nuclear science*, 50(5):1664–1666.

[Firsching, 2005] Firsching, M. (2005). Die methode der materialrekonstruktion in der energieaufgeloesten roentgenbildgebung. Master's thesis, Physikalisches Institut der Friedrich-Alexander-Universitaet, Erlangen-Nuernberg.

[Firsching et al., 2004] Firsching, M., Giersch, J., Niederloehner, D., and Anton, G. (2004). A method for stoichiometric material reconstruction with spectroscopic x-ray pixel detectors. *Proceedings Nuclear Science Symposium*, pages 4116–4119.

[Firsching et al., 2007] Firsching, M., Michel, T., and Anton, G. (2007). First measurements of material reconstruction in x-ray imaging with the medipix2 detector. *Proceedings Nuclear Science Symposium, Honolulu*, 4:2736–2740.

[Giersch et al., 2004] Giersch, J., Niederloeher, D., and Anton, G. (2004). The influence of energy weighting on x-ray imaging quality. *Nuclear Instruments and Methods in Physics Research A*, 531:68–74.

[Gleason et al., 1999] Gleason, S., Sari-Sarraf, H., Paulus, M., Johnson, D., Norton, S., and Abidi, M. (1999). Reconstruction of multi-energy x-ray computed tomography images of laboratory mice. *IEEE Transactions on Nuclear Science*, 46(4):1081–1086.

[Graser et al., 2008] Graser, A., Johnson, T. R. C., Chandarana, H., and Macari, M. (2008). Dual energy ct: preliminary observations and potential clinical applications in the abdomen. *European Radiology*.

[Holy et al., 2006] Holy, T., Jakubek, J., Pospisil, S., Uher, J., Vavrik, D., and Vykydal, Z. (2006). Data acquisition and processing software package for medipix2. *Nuclear Instruments and Methods in Physics Research Section A*, 563:254–258.

[Johnson et al., 2007] Johnson, T., Krauss, B., Sedlmair, M., Grasruck, M., Bruder, H., Morhard, D., Fink, C., Weckbach, S., Lenhard, M., Schmidt, B., Flohr, T., Reiser, M., and Becker, C. (2007). Material differentiation by dual energy ct: initial experience. *European Radiology*, 17:1510–1517.

[Jollife, 2002] Jollife, I. (2002). *Principal Component Analysis*. Springer-Verlag, 2nd edition.

[Kalukin et al., 2000] Kalukin, A. R., Van Geet, M., and Swennen, R. (2000). Principal component analysis of multienergy x-ray computed tomography of mineral samples. *IEEE Transactions on Nuclear Science*, 47(5):1729–1736.

[Karg, 2006] Karg, J. (2006). Energiegewichtung in der roentgenbildgebung: Ein neues verfahren zur verbesserung der bildqualitaet. Master's thesis, Physikalisches Institut der Friedrich-Alexander-Universitaet, Erlangen-Nuernberg.

[Llopart, 2006] Llopart, X. (2006). *MPIX2MXR20 Manual v2.3.* http://medipix.web.cern.ch/MEDIPIX/Medipix2/PasswordProtected /Documents/MXR/Mpix2MXR20%20Documentv2.3.pdf.

[Llopart et al., 2007] Llopart, X., Ballabriga, R., Campbell, M., Tlustos, L., and Wong, W. (2007). Timepix, a 65k programmable pixel readout chip for arrival time, energy and/or photon counting measurements. *Nuclear Instruments and Methods in Physics Research Section A*, 581:485–494.

[Mehl et al., 2004] Mehl, P. M., Chen, Y.-R., Kim, M. S., and Chan, D. E. (2004). Development of hyperspectral imaging technique for the detection of apple surface defects and contaminations. *Journal of Food Engineering*, 61:67–81.

[Mitschke, 2006] Mitschke, M. (2006). *Evaluation of different sensor materials for the medipix X-ray detectors.* PhD thesis, Physikalisches Institut der Friedrich-Alexander-Universitaet, Erlangen-Nuernberg.

[Niederloehner, 2006] Niederloehner, D. (2006). *Untersuchungen zur Energiewichtung in der medizinischen Roentgenbildgebung mit dem Medipix2-Detektor.* PhD thesis, Physikalisches Institut der Friedrich-Alexander-Universitaet, Erlangen-Nuernberg.

[Niederloehner et al., 2005] Niederloehner, D., Nachtrab, F., Michel, T., and Anton, G. (2005). Using the medipix2 detector for photon counting computed tomography. *IEEE Nuclear Science Symposium Conference Record*, pages 2327–2331.

[Radon, 1917] Radon, J. (1917). Über die bestimmung von funktionen durch ihre integralwerte längs gewisser mannigfaltigkeiten. *Ber. Sächs. Akad. Wissenschaft., Leipzig Math. Phys. Kl.*, 69:262–267.

[Roessl and Proksa, 2007] Roessl, E. and Proksa, R. (2007). K-edge imaging in x-ray computed tomography using multi-bin photon counting detectors. *Physics in Medicine and Biology*, 52(15):4679–4696.

[Scheffel et al., 2006] Scheffel, H., Alkadhi, H., Plass, A., Vachenauer, R., Desbiolles, L., Gaemperli, O., Schepis, T., Frauenfelder, T., Schertler, T., Husmann, L., Grunenfelder, J., Genoni, M., Kaufmann, P. A., Marincek, B., and Leschka, S. (2006). Accuracy of dual-source ct coronary angiography: first experience in a high pre-test probability population without heart rate control. *European Radiology*, pages 2739–2747.

[Stephan et al., 2008] Stephan, K., Hibbitts, C., Hoffmann, H., and Jaumann, R. (2008). Reduction of instrument-dependent noise in hyperspectral image data using the principal component analysis: Applications to galileo nims data. *Planetary and Space Science*, 56:406–419.

[Uher et al., 2008] Uher, J., Jakubek, J., Koster, U., Lebel, C., Leroy, C., Pospisil, S., Skoda, R., and Vykydal, Z. (2008). Detection of fast neutrons with the medipix-2 pixel detector. *Nuclear Instruments and Methods in Physics Research Section A*, 591:71–74.

[Winson et al., 1997] Winson, M. K., Goodacre, R., Éadaoin M. Timmins, Jones, A., Alsberg, B. K., Woodward, A. M., Rowland, J. J., and Kell, D. B. (1997). Diffuse reflectance absorbance spectroscopy taking in chemometrics (drastic). a hyperspectral ft-ir-based approach to rapid screening for metabolite overproduction. *Analytica Chimica Acta*, 348:273–282.

[Zhang et al., 2008] Zhang, L. J., Yang, G. F., and Lu, G. M. (2008). Noninvasive diagnosis of bronchial artery aneurysm using dual-source computed tomography angiography. *Acta Radiologica*, 49:291–294.